Galaxy Formation in Sterile Neutrino Dark Matter Models

N. Menci[1] ⓘ, A. Grazian[1] ⓘ, A. Lamastra[1,2], F. Calura[3] ⓘ, M. Castellano[1] ⓘ, and P. Santini[1] ⓘ
[1] INAF—Osservatorio Astronomico di Roma, via Frascati 33, I-00078 Monteporzio, Italy
[2] Space Science Data Center—ASI, via del Politecnico SNC, I-00133 Roma, Italy
[3] INAF—Osservatorio Astronomico di Bologna, Via Gobetti 93/3, I-40129 Bologna, Italy

Abstract

We investigate galaxy formation in models with dark matter (DM) constituted by sterile neutrinos. Given their large parameter space, defined by the combinations of sterile neutrino mass m_ν and mixing parameter $\sin^2(2\theta)$ with active neutrinos, we focus on models with $m_\nu = 7$ keV, consistent with the tentative 3.5 keV line detected in several X-ray spectra of clusters and galaxies. We consider (1) two resonant production models with $\sin^2(2\theta) = 5 \times 10^{-11}$ and $\sin^2(2\theta) = 2 \times 10^{-10}$, to cover the range of mixing parameters consistent with the 3.5 keV line; (2) two scalar-decay models, representative of the two possible cases characterizing such a scenario: a freeze-in and a freeze-out case. We also consider thermal warm DM with particle mass $m_X = 3$ keV. Using a semianalytic model, we compare the predictions for the different DM scenarios with a wide set of observables. We find that comparing the predicted evolution of the stellar mass function, the abundance of satellites of Milky Way–like galaxies, and the global star formation history of galaxies with observations does not allow us to disentangle the effects of the baryonic physics from those related to the different DM models. On the other hand, the distribution of the stellar-to-halo mass ratios, the abundance of faint galaxies in the UV luminosity function at $z \gtrsim 6$, and the specific star formation and age distribution of local, low-mass galaxies constitute potential probes for the DM scenarios considered. We discuss how future observations with upcoming facilities will enable us to rule out or to strongly support DM models based on sterile neutrinos.

Key words: dark matter – galaxies: evolution – galaxies: formation

1. Introduction

Dark matter (DM) is the main driver of galaxy formation. Its nature defines the power spectrum of density fluctuations that collapse to form cosmic structures, thus determining the abundance and the properties of galaxies at the different mass scales. For example, the standard cold dark matter (CDM) scenario is based on candidates constituted by massive ($m_X > 0.1$ GeV) thermal relics (WIMPS) or condensates of light axions (with mass $\sim 10^{-5}$–10^{-1} eV), characterized by thermal velocities small enough to make density perturbations gravitationally unstable down to mass scales negligible for galaxy formation. Correspondingly, the rms amplitude of density fluctuations continues to increase for decreasing mass scales, yielding an ever-increasing abundance of dwarf galaxies down to subgalactic mass scales ($M \approx 10^7$–$10^9 M_\odot$). However, several observations concerning the dwarf galaxy population seem to challenge such a scenario (see Bullock & Boylan-Kolchin 2017 for a recent review and for a complete account of the existing literature). For example, the predicted abundance of low-mass DM halos is much larger than the observed abundance of dwarf galaxies. The issue is most acute for satellite galaxies (Klypin et al. 1999; Moore et al. 1999; Diemand et al. 2008; Springel et al. 2008), but is present also in the field (see, e.g., Zavala et al. 2009; Schneider et al. 2017b). A possible solution can be sought in the effects of feedback from supernovae (e.g., Larson 1974) and from the UV background (e.g., Efstathiou 1992), which can suppress or even prevent (see, e.g., Sawala et al. 2016) star formation in low-mass galaxies, thus strongly reducing the number of luminous galaxies in CDM models, bringing them in closer agreement with observations (see, e.g., Garrison-Kimmel et al. 2017). However, such a suppression of the baryon-to-DM content of galaxies can potentially lead to a tension with the observed values. In fact, the kinematics of dwarf galaxies (with stellar masses $M_* = 10^6$–$10^8 M_\odot$) indicate that they are hosted by DM halos with mass smaller than predicted by CDM models (Ferrero et al. 2012; Garrison-Kimmel et al. 2014; Papastergis et al. 2015; Papastergis & Shankar 2016).

While the possibility that feedback effects can provide a simultaneous solution to all of the above issues within the CDM framework is still a matter of debate, increasing attention is being devoted to alternative DM models with suppressed power spectra at small galactic scales of $M \approx 10^8$–$10^9 M_\odot$ with respect to the CDM case. This is also motivated by the fact that both direct (Aprile et al. 2012, 2016, Akerib et al. 2014) and indirect (see, e.g., Adriani et al. 2013; Ackermann et al. 2015) DM detection experiments have failed to provide a definite confirmation of the CDM scenario. Also, no evidence for CDM candidates with mass 10^2–10^4 GeV has been found in experiments at LHC (see, e.g., Ade et al. 2016), while experiments aimed at detecting axions as DM components have produced no evidence in the explored portion of the parameter space (Graham et al. 2015; Marsh 2016).

The combination of astrophysical issues with the lack of detection of CDM candidates has motivated several groups to investigate galaxy formation in a number of alternative models. Among the proposed DM candidates, a prominent class is constituted by models that assume DM to be constituted by lighter particles with mass m_X in the kiloelectronvolt range (see de Vega & Sanchez 2010). The simpler assumption is to consider such particles to be thermal relics (warm dark matter, WDM; see Bode et al. 2001) resulting from the freeze-out of particles initially in thermal equilibrium in the early universe (like gravitinos; see Steffen 2006 for a review). Their larger thermal velocities (corresponding to larger free-streaming lengths) suppress structure formation at scales $M = 10^7$–$10^9 M_\odot$,

depending only on the value of m_X (since a thermalized species has no memory of the details of its production). Such a one-to-one correspondence between the WDM particle mass and the suppression in the power spectrum at small scales has allowed us to derive limits on m_X by comparing the predictions from N-body WDM simulations or semianalytic models (SAMs) with the abundance of observed ultrafaint galaxies. On this basis, different authors have derived limits ranging from $m_X \geqslant 1.5$ keV (Lovell et al. 2012) to $m_X \geqslant 1.8$ keV (Horiuchi et al. 2014), $m_X \geqslant 2$ keV (Kennedy et al. 2014), and $m_X \geqslant 2.3$ keV (Polisensky & Ricotti 2011) from the abundance of local dwarf satellites, while at higher redshifts, $z \approx 6$, a limit $m_X \gtrsim 1.5$ keV has been derived from the UV luminosity functions of faint galaxies down to $M_{UV} \approx -16$ (Schultz et al. 2014; Corasaniti et al. 2017). The tighter constraints achieved so far of $m_X \geqslant 3.3$ keV (at 2σ c.l.) for WDM thermal relics are derived by comparing small-scale structure in the Lyα forest of high-resolution ($z > 4$) quasar spectra with hydrodynamical N-body simulations (Viel et al. 2013). While all of the above methods are affected by uncertainties related to baryon physics, a baryon-independent limit of $m_X \geqslant 2.5$ keV (2σ c.l.) has been derived by Menci et al. (2016) from the abundance of $z = 6$ galaxies observed by Livermore et al. (2017; see also Bouwens et al. 2017b). The overall result from the studies above is that a limit $m_X \gtrsim 2.5$–3 keV for thermal WDM candidates constitutes a rather robust indication.

An alternative possibility for kiloelectronvolt-scale DM is constituted by models based on sterile neutrinos (SNs hereafter). In such scenarios, the power spectra are nonthermal and depend not only on the assumed mass of the SN m_ν but also on the the production mechanism. In particular, for SNs produced from oscillations of active neutrinos, the power spectrum depends also on the mixing angle θ defining the admixtures $\sin^2(2\theta)$ with the active neutrinos. While earlier models (Dodelson & Widrow 1994) required relatively large mixing angles to produce the observed abundance of DM, more recent scenarios assume an enhancement due to resonant production in the presence of a nonvanishing lepton asymmetry (Shi & Fuller 1999), thus allowing for extremely small mixing angles of $\sin^2(2\theta) \leqslant 10^{-9}$. These models have received particular interest in the literature in recent years (see Adhikari et al. 2017 for a complete review). This is due to both solid fundamental physics motivations (right-handed neutrinos constitute a natural extension of the Standard Model to provide mass terms for active neutrinos; see Merle 2013) and to the fact that such particles constitute the simplest candidates (see, e.g., Abazajian 2014) for a DM interpretation of the potential X-ray line at energy $E \approx 3.5$ keV in stacked observations of galaxy clusters and in the Perseus cluster with the *Chandra* observatory (Bulbul et al. 2014); independent indications of a consistent line in *XMM-Newton* observations of M31 and the Perseus Cluster (Boyarsky et al. 2014) have been followed by measurements in different objects (the Galactic center and other individual clusters, Iakubovskyi 2016 measurements of the cosmic X-ray background toward the COSMOS Legacy and CDFS survey fields, Cappelluti et al. 2017) and from other observatories like *Suzaku* (Urban et al. 2015; Franse et al. 2016) and *NuSTAR* (observations of the COSMOS and Extended *Chandra* Deep Field South survey fields; Neronov et al. 2016). In fact, the tiny admixtures $\sin^2(2\theta)$ with the active neutrinos allow the decay of SNs, resulting in photon emission at energies close to $m_\nu/2$ with emission $F \propto \sin^2(2\theta)$. The

nondetection of such a line in several systems (see, e.g., Anderson et al. 2015; Malyshev et al. 2014; Adhikari et al. 2017; Bulbul et al. 2016; Ruchayskiy et al. 2016 for an extended discussion) yields effective *upper* limits on the mixing angle as a function of m_ν. For example, for $m_\nu = 7$ keV (the value consistent with the tentative 3.5 keV line), nondetections yield a limit $\log \sin^2(2\theta) \lesssim -9.7$; while still consistent with the range of values corresponding to the tentative 3.5 keV line ($-10.6 \leqslant \log \sin^2(2\theta) \leqslant -9.5$), such a limit from nondetections is effective in ruling out sterile neutrino models based on the nonresonant production mechanism of Dodelson & Widrow (1994). Thus, the present observational situation leaves open the possibility for sterile neutrino models based on resonant production by oscillations with active neutrinos (RP models; Shi & Fuller 1999), and to models in which SNs are produced by the decay of a scalar particle (SD), presented in detail in Merle & Totzauer (2015 and references therein).

Given the interest in the above DM models with suppressed power spectra, several studies of galaxy formation have been carried out in WDM scenarios using either SAMs (Menci et al. 2012, 2013, Benson et al. 2013; Kang et al. 2013; Nierenberg et al. 2013; Dayal et al. 2015; Bose et al. 2017) or hydrodynamical simulations (Herpich et al. 2014; Maio & Viel 2015; Lovell et al. 2016; Wang et al. 2017), addressing the global galaxy properties (like luminosity and stellar mass functions and galaxy star formation) and the properties of satellite galaxies around Milky Way–like galaxies in WDM scenarios with m_X ranging from 1 to 3 keV. However, a global exploration of galaxy formation in sterile neutrino DM scenarios is still missing, although the investigation of specific issues has been undertaken using high-resolution simulations (Bose et al. 2017; Lovell et al. 2016, 2017a, 2017b). In this paper, we tackle this task by exploring the impact of assuming different existing sterile neutrino DM models on the observable properties of galaxies, including stellar mass and luminosity functions, satellite abundances, L/M ratios, and star formation properties. To this aim, we use a state-of-the-art SAM (see Somerville & Davé 2015 for a review) with different initial power spectra, each corresponding to a selected sterile neutrino model. Given the large parameter space of such DM models, determined by the possible combination of sterile neutrino mass m_ν and mixing parameter $\sin^2(2\theta)$, we choose to focus this work on models with fixed sterile neutrino mass $m_\nu = 7$ keV, that is, on models that can be consistent with the tentative 3.5 keV line in the X-ray spectra of clusters and galaxies discussed above. In particular, we consider (1) two RP models of SNs with mixing angles $\sin^2(2\theta) = 5 \times 10^{-11}$ and $\sin^2(2\theta) = 2 \times 10^{-10}$, to cover the range of mixing parameters consistent with the tentative 3.5 keV line; and (2) two SD models representative of the two possible cases characterizing such a scenario: a freeze-in and a freeze-out case (see Section 2 for further details). For comparison, we also show our prediction for the CDM case and for thermal WDM with mass $m_X = 3$ keV.

The paper is organized as follows. In Section 2 we describe the model setup: Section 2.1 provides a brief description of the SN models we consider; in Section 2.2 we describe how we implement such DM models in our SAM; and in Section 2.3 we recall how the baryonic processes affecting galaxy formation are described in the SAM, and we present our strategy to fix the model free parameters. In Section 3 we
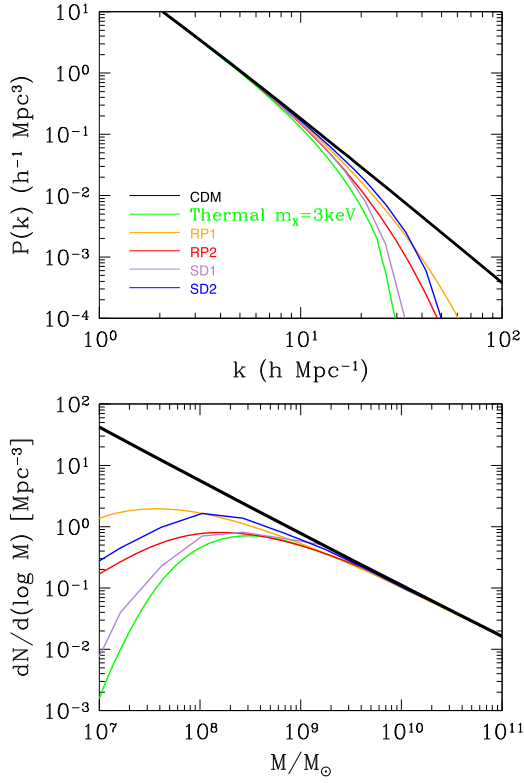
Figure 1. Upper panel: the linear power spectrum at $z = 0$ for the different DM models considered in the text, as indicated by the labels. Lower panel: for the same DM models, we show the DM halo mass function at $z = 0$.

present our results concerning the local properties of DM halos (Section 3.1, satellite abundance, stellar-to-halo mass ratios), the evolution of the galaxy population (Section 3.2, evolution of the stellar mass and luminosity distributions), and star formation (Section 3.3, specific star formation, star formation histories, ages of stellar populations, colors). The aim is to investigate to what extent the comparison with the different observables can help to disentangle the effects of baryon physics (in particular of feedback) from the specific effects of the different assumed DM models. Section 4 is devoted to discussion and conclusions.

Throughout the paper, round "concordance cosmology" values have been assumed for the cosmological parameters: Hubble constant $h = 0.7$ in units of $100 \, \mathrm{km \, s^{-1} \, Mpc^{-1}}$, total matter density parameter $\Omega_0 = 0.3$, and baryon density parameter $\Omega_b = 0.045$.

2. The Model

2.1. Dark Matter Scenarios

The evolution of the DM condensations on spatial scales r is determined by the power spectrum $P(k)$ of DM perturbations (in terms of the wavenumber $k = 2\pi/r$) that can be computed from the momentum distribution function of the DM. As discussed in the Introduction, we consider five DM models besides CDM, chosen to yield appreciable suppression in the power spectrum with respect to CDM but still consistent (albeit marginally) with existing bounds from X-ray observations and structure formation; thus the corresponding power spectra (shown in Figure 1) constitute a representative set of different possible forms for such borderline cases. In detail, we consider the following DM models:

1. CDM: In this case we adopt the power spectrum $P_{\mathrm{CDM}}(k)$ given in Bardeen et al. (1986).
2. Thermal WDM with particle mass $m_X = 3$ keV: In this case, the suppression of power spectrum $P(k)$ with respect to the CDM case is $P(k)/P_{\mathrm{CDM}}(k) = [1 + (\alpha \, k)^{2 \, \mu}]^{-10/\mu}$ with $\alpha = 0.049[\Omega_X/0.25]^{0.11} [m_X/\mathrm{keV}]^{-1.11} [h/0.7]^{1.22} \, h^{-1}$ Mpc and $\mu = 1.12$ (Bode et al. 2001; see also Viel et al. 2006; Destri et al. 2013). As noted in the Introduction, for thermal WDM, the spectrum depends solely on the assumed particle mass m_X. For our assumed mass $m_X = 3$ keV, the WDM spectrum is suppressed by one-half with respect to CDM at the half-mode mass scale $M_{1/2} = 4 \cdot 10^8 \, h^{-1} \, M_\odot$, with the suppression rapidly increasing at smaller masses (see Figure 1).
3. RP1 model: Resonantly produced sterile neutrinos with $m_\nu = 7$ keV and $\sin^2(2\theta) = 2 \times 10^{-10}$. Since for each combination of m_ν and $\sin^2(2\theta)$ the lepton asymmetry is fixed to the value required to yield the right DM abundance, our choice corresponds to a lepton asymmetry $L_6 \approx 8$ (in units of 10^{-6}; see, e.g., Boyarsky et al. 2009; Abazajian 2014). The momentum distribution strongly differs from a generic Fermi–Dirac form and is computed with the public code *sterile-dm* of Venumadhav et al. (2016; for an extended analysis see also Ghiglieri & Laine 2015). The computation is based on the Boltzmann equation and includes detailed calculations of the lepton asymmetry around the quark–hadron transition. To obtain the power spectrum, the publicly available Boltzmann solver *CLASS* (Blas et al. 2011) has been used (Menci et al. 2017).
4. RP2 model: As above, but with $\sin^2(2\theta) = 5 \times 10^{-11}$, corresponding to $L_6 \approx 10$. The spectrum is computed with the same tools described above.
5. SD1: Scalar-decay model with $m_\nu = 7$ and freeze-in regime (see König et al. 2016 for an extended discussion). Production from scalar decay is described by a generic model that invokes one real scalar singlet S and one sterile neutrino N beyond the Standard Model. The interaction between the scalar and the sterile neutrino is encoded in $\mathcal{L} \supset -\frac{y}{2} S \overline{N^c} N$, where y is a Yukawa-type coupling determining the decay rate of the scalar and hence controlling how fast the scalar decays into sterile neutrinos. If the scalar develops a nonzero expectation value $\langle S \rangle$, this leads to a Majorana mass $m_\nu = y \langle S \rangle$. For a scalar with $\langle S \rangle$ in the GeV–TeV range, couplings $y \approx 10^{-9}$–10^{-5} are required to have $m_\nu \sim$ keV. The scalar singlet couples to the Higgs doublet Φ via a *Higgs portal* $\mathcal{L} \supset 2\lambda(\Phi^\dagger \Phi) S^2$, where λ is a dimensionless coupling that determines the production rate of the scalar. In the limit of small Higgs portal couplings ($\log \lambda \ll -6$), the scalar itself is produced by freeze-in (at least when y is within the range explored here; see Heikinheimo et al. 2017 for more extended cases) and is always strongly suppressed compared to its would-be equilibrium abundance. As a representative case of this class of models, we consider the case $y = 10^{-8.5}$, $\lambda = 10^{-8}$, with $m_S = 100$ GeV, which —although yielding an appreciably suppressed power spectrum with respect to CDM—is marginally consistent with existing bounds from X-ray observations and from structure formation (Merle & Totzauer 2015). The momentum distributions are derived in König et al. (2016), and the power spectrum is calculated with the Boltzmann solver *CLASS* as in Menci et al. (2017).

6. SD2: Scalar-decay model with $m_\nu = 7$ and freeze-out regime. The framework is the same outlined above, but in this case λ is large enough to equilibrate the scalars so that they will be subject to the well-known dynamics of freeze-out. We shall consider the case $m_S = 100$ GeV, $y = 10^{-8.5}$, $\lambda = 10^{-5}$ as a borderline case (with substantial suppression of the power spectrum with respect to CDM and still marginally consistent with existing bounds; see Merle & Totzauer 2015) representative of this class of models.

The models considered are summarized in Table 1, where we show key quantities characterizing the suppression of the power spectrum compared to the CDM case: the half-mode mass $M_{1/2}$, and the wavenumber k_{peak} at which the dimensionless power spectrum $k^3 P(k)$ peaks. In the table we also indicate the values of the parameters v_0 and α defining the supernova feedback adopted for each model, as described in detail in Section 2.3.

2.2. The Semianalytic Model: The Dark Matter Sector

The backbone of the computation is constituted by the collapse history of DM halos on progressively larger scales. Realizations of such histories are generated through a Monte Carlo procedure on the basis of the merging rates given by the extended Press and Schechter (EPS) theory; see Bond et al. (1991), Bower (1991), and Lacey & Cole (1993). In this framework, the evolution of the DM condensations is determined by the power spectrum $P(k)$, which is computed for the considered DM models as described in Section 2.1, through the variance σ of the primordial DM density field. This is a function of the mass scale $M \propto \overline{\rho} r^3$ of the DM density perturbations (and of the background density $\overline{\rho}$) given by

$$\sigma^2(M) = \int \frac{dk\, k^2}{2\,\pi^2} P(k) W(kr), \tag{1}$$

where $W(kr)$ is the window function (see Peebles 1993). While for CDM a top-hat shape in the real space is the canonical choice for the filter function, both theoretical arguments (Benson et al. 2013; Schneider et al. 2013) and numerical experiments (see Schneider et al. 2012, 2013; Angulo et al. 2013) show that the proper choice for models with suppressed power $P(k)$ at large k is constituted by a sharp-k form (a top-hat sphere in Fourier space). While for a top-hat filter the mass assigned to the scale r is $M = 4\pi \overline{\rho} r^3/3$, in the case of a sharp-k filter, the mass assigned to the filter scale is calibrated with simulations. These show that by adopting the relation $M = 4\pi \overline{\rho}(cr)^3/3$ with $c = 2.7$ (Schneider et al. 2013), the resulting mass distributions provide an excellent fit to N-body results for a wide range of DM masses and redshifts (see Schneider 2015).

The differential halo mass function of DM halos (per unit $\log M$) can be calculated based on the extended Press and Schechter approach (Benson et al. 2013; Schneider et al. 2013):

$$\frac{d\phi}{d\ln M} = \frac{1}{6}\frac{\overline{\rho}}{M} f(\nu) \frac{d\ln \sigma^2}{d\ln r} = -\frac{1}{2\,\pi^2\,\sigma^2(r)} \frac{P(1/r)}{r^3}, \tag{2}$$

where the latter equality applies when the variance is computed adopting a sharp-k filter. Here $\nu \equiv \delta_c^2(t)/\sigma^2$ depends on the linearly extrapolated density for collapse in the spherical

model, $\delta_c(t) = 1.686/D(t)$, and $D(t)$ is the growth factor of DM perturbations. We conservatively assume a spherical collapse model, for which $f(\nu) = \sqrt{2\nu/\pi}\,\exp(-\nu/2)$. The effect of assuming different power spectra (corresponding to the different DM models introduced in Section 2.1) on the differential halo mass function is shown in the bottom panel of Figure 1.

The merging trees of DM halos are generated through a Monte Carlo procedure (as described in Menci et al. 2005 and references therein) from the conditional mass function, which gives the abundance of halos per mass M and cosmic time t, eventually ending up in a single host halo with mass M_0 at final time t_0. In the case of a sharp-k filter (adopted for our models with suppressed power spectra), this reads (Benson et al. 2013; Schneider 2015)

$$\frac{dN(M|M_0)}{d\ln M} = \frac{1}{6\,\pi^2}\frac{M_0}{M} f(\delta_c, M|\delta_{c,0}, M_0)\frac{P(1/r)}{r^3},$$

where the conditional first-crossing distribution in the case of spherical collapse is given by

$$f(\delta_c, S|\delta_{c,0}, S_0) = \frac{\delta_c(t) - \delta_{c,0}}{\sqrt{2\,\pi\,[\sigma^2(M) - \sigma^2(M_0)]}}\, e^{-\frac{[(\delta_c(t)-\delta_{c,0}]^2}{2\,\pi\,[\sigma^2(M)-\sigma^2(M_0)]}}.$$

The merging histories generated by the above Monte Carlo procedure allow us to track the merging histories of DM clumps down to the mass $M = 10^7 M_\odot$, well below the half-mode mass scale characterizing the suppression in the power spectrum of the considered DM models with respect to CDM.

The dynamical evolution of substructures is computed in our Monte Carlo procedure as described in detail in Menci et al. (2005, 2008). After each merging event, the DM halos included in a larger object may survive as satellites or sink to the center due to dynamical friction to increase the mass of the central dominant galaxy. The density profiles of DM halos have been computed using a Navarro, Frenk, and White (NFW; 1997) form. The mass dependence of the concentration parameter c (M) has been taken from Macció et al. (2008) for the CDM case. For the DM models with suppressed power spectra, we computed $c(M)$ using the algorithm in Schneider (2015), yielding a downturn of $c(M)$ for mass scales smaller than the half-mode mass scale $M \lesssim M_{1/2}$.

2.3. The Semianalytic Model: The Baryonic Sector and the Setting of Free Parameters

The baryonic processes taking place in each dark matter halo are computed as described in earlier works (see Menci et al. 2014, and references therein). The gas in the halo, initially set to have a density given by the universal baryon fraction and to be at the virial temperature, cools by atomic processes and settles into a rotationally supported disk with mass M_{gas}, disk radius r_d, and disk circular velocity v_d, computed as in Mo et al. (1998). The cooled gas M_{gas} is gradually converted into stars, with a star formation rate (SFR) $\dot{M}_* = M_{\mathrm{gas}}/\tau_*$ given by the Schmidt–Kennicutt law with a gas conversion timescale $\tau_* = q\,\tau_d$ proportional to the dynamical timescale τ_d through the free parameter q. In addition to the above "quiescent" mode of star formation, galaxy interactions occurring in the same host dark matter halo may induce the sudden conversion of a fraction f of cold gas into stars on a short timescale of $\sim 10^7$–10^8 years given by the duration of the interaction. The fraction f is related to the mass ratio and to the

Table 1
Dark Matter Models Considered and Corresponding Key Quantities

| Model	DM Particle	Model Parameters	$M_{\rm hm}$ ($10^8 \, h^{-1} \, M_\odot$)	$k_{\rm peak}$ (h Mpc^{-1})	v_0 (km s^{-1})	α
CDM	Cold relics				300	3.3
WDM	Warm thermal relics	Relic particle mass $m_X = 3$ keV	4	7.6	340	2
RP1	Resonantly produced sterile neutrinos. Large mixing angle.	Sterile neutrino mass $m_\nu = 7$ keV; Mixing parameter $\sin^2(2\theta) = 2 \times 10^{-10}$	2.6	10.7	360	2
RP2	Resonantly produced sterile neutrinos. Small mixing angle.	Sterile neutrino mass $m_\nu = 7$ keV; Mixing parameter $\sin^2(2\theta) = 5 \times 10^{-11}$	2.9	8.9	340	2
SD1	Sterile neutrinos produced via scalar decay in a freeze-in regime.	Sterile neutrino mass $m_\nu = 7$ keV; Scalar coupling with Higgs sector $\lambda = 10^{-8}$; Scalar coupling with sterile neutrino $y = 10^{-8.5}$; Scalar particle mass $m_S = 100$ GeV	3	9.1	340	2
SD2	Sterile neutrinos produced via scalar decay in a freeze-out regime.	Sterile neutrino mass $m_\nu = 7$ keV; Scalar coupling with Higgs sector $\lambda = 10^{-5}$; Scalar coupling with sterile neutrino $y = 10^{-8.5}$; Scalar particle mass $m_S = 100$ GeV	1.6	13.5	360	2
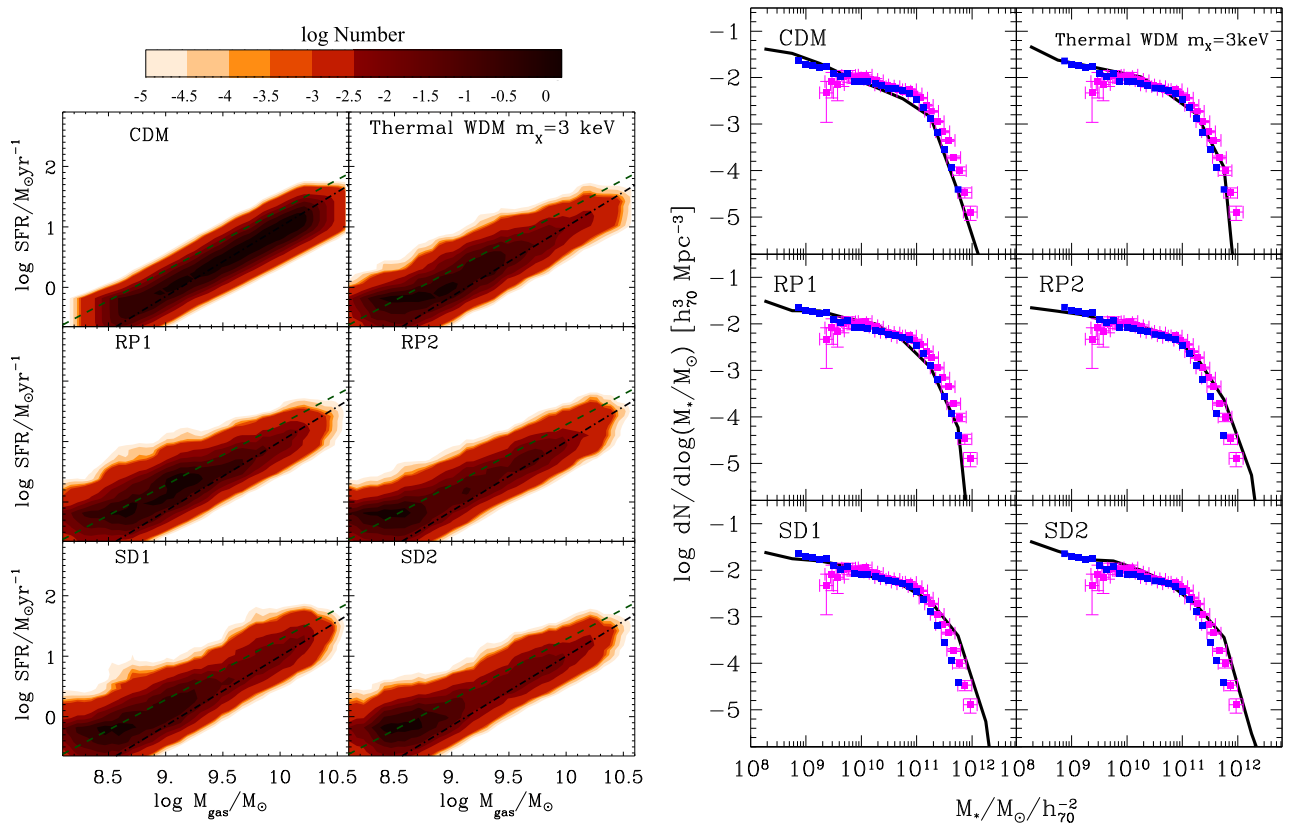
Figure 2. Left panels: the relation between the star formation rate and the disk gas component; the contours show the distribution of model galaxies for the different DM models indicated by the labels. The lines correspond to the fit relation given in Equation (8) of Santini et al. (2014, dashed line) and in Genzel et al. (2010, dashed–dotted line). The color code corresponds to the logarithm of the number of galaxies in each point of the SFR–M_{gas} plane normalized to the maximum value, as shown by the color bar. Right panels: The local stellar mass function obtained from model galaxies in the different DM scenarios (solid line) are compared with data from Baldry et al. (2012, blue squares) and Li & White (2009, pink squares).

relative velocity of the merging partners, as described in Menci et al. (2003). The energy released by the supernovae associated with the total star formation returns a fraction of the disk gas into the hot phase, at a rate $\dot{M}_h = \dot{M}_*/(v_d/v_0)^\alpha$ parameterized (as in most SAMs; see, e.g., Cole et al. 2000; Benson et al. 2003; Gonzalez-Perez et al. 2014; see also the review by Somerville & Davé 2015) in terms of the free parameters v_0 and α, defining the normalization and the scaling of the feedback efficiency with the size of the host DM halo, respectively. Following existing works based on SAMs (see, e.g., Benson et al. 2003; Font et al. 2011), we model reionization feedback using a simple approximation in which dark matter halos with circular velocity at the virial radius $v \leqslant v_{crit}$ have no gas accretion or gas cooling at redshifts smaller than that corresponding to reionization $z \leqslant z_{cut}$. We take $v_{crit} = 25 \text{ km s}^{-1}$ (see, e.g., Okamoto et al. 2008; see also Hou et al. 2016) and $z_{cut} = 10$ (see, e.g., Benson et al. 2003; Kennedy et al. 2014); varying the assumed z_{cut} in the range 7–10 does not appreciably change our main results. This simple model provides a good approximation to more complex, self-consistent photoionization feedback models (Benson et al. 2002; Font et al. 2011) and is widely adopted in SAMs (see, e.g., Hou et al. 2016), including recent works on the comparison between CDM and WDM predictions (see Kennedy et al. 2014).

An additional source of feedback is provided by the energy radiated by the active galactic nuclei (AGNs) that correspond to the active accretion phase of the supermassive black hole at the center of DM halos. The detailed description of our implementation of the AGN feedback is given in Menci et al.

(2008); this, however, mainly affects the massive galaxy population, which is not our main focus here. Finally, the luminosity—in different bands—produced by the stellar populations of the galaxies are computed by convolving the star formation histories of the galaxy progenitors with a synthetic spectral energy distribution, which we take from Bruzual & Charlot (2003) assuming a Salpeter IMF. The model also includes a treatment of the transfer of stellar mass to the bulge during mergers and the tidal stripping of stellar material from satellite galaxies, as described in detail in Menci et al. (2014).

The main free parameters in the modes are the normalization of the star formation timescale q and the feedback normalization and scaling, v_0 and α. For each considered DM model, we choose the first so as to reproduce the observed correlation between the SFR and the gas mass (Figure 2, left panels), while v_0 and α are calibrated to match the shape of the low-mass end of the local stellar mass function (Figure 2, right panels).

We find that we can keep the same star formation efficiency adopted in our earlier works $q = 20$ for all of the different DM models, while matching the local stellar mass function (Figure 2, right panels) requires different values of the feedback parameter for the different DM models: while for CDM we take $\alpha = 3.3$ and $v_0 = 300 \text{ km s}^{-1}$, for the models with a suppressed power spectrum, we take $\alpha = 2$ with $v_0/\text{km s}^{-1} = 340, 360, 340, 340, 360$ for models WDM, RP1, RP2, SD1, SD2, respectively. This is because the lower abundance of low-mass halos in WDM and SN models compared to CDM allows us to match the flat logarithmic

slope of the faint end of the observed stellar mass function with a milder feedback (a combination that seems to provide a slightly better match to the data compared to CDM, although the precise fit depends on the details of the baryon physics). The different combinations of feedback parameters adopted for the considered DM models are summarized in the rightmost columns of Table 1.

Our approach and the values of the feedback free parameters are similar to those adopted in previous works (see, e.g., Kennedy et al. 2014) and correspond to implementing weaker stellar feedback in DM models with a suppressed power spectrum, since the lower abundance of low-mass galaxies in such models allows us to match the local stellar mass function with a milder suppression of the L/M (or M_*/M) ratio. Thus, matching the abundance of low-mass halos results in larger effective star formation in low-mass halos in models with a suppressed power spectrum, as found in previous works based on an abundance-matching technique (see Corasaniti et al. 2017). In the following, we will investigate to what extent the different observables we compare with enable us to disentangle the effects of feedback from those related to the assumed DM spectrum.

3. Results

Based on the SAM described above, we compute the observable properties of galaxies at low and high redshift, and we compare with available data, focusing our comparison on the low-mass end ($M \leqslant 10^9 M_\odot$) of the galaxy distribution, the one more affected by the suppression in the power spectrum yield by the SN DM models. We aim to investigate to what extent the comparison with the different observables can help us to disentangle the effects of baryon physics (in particular of feedback) from the specific effects of the different assumed DM models, and to single out the observational properties of low-mass galaxies that can potentially constitute a robust probe to strongly support or to rule out the considered SN models.

3.1. Local Properties of DM Halos

We first compare the predictions of the considered DM models with the abundance of satellites of Milky Way–like galaxies (Figure 3). In fact, this has long been a major issue for CDM (Klypin et al. 1999; Moore et al. 1999), due to the large number of predicted subhalos compared with the observed number of visible satellite galaxies. However, dwarf satellite galaxies are also quite sensitive to the effect of baryonic feedback to supernovae and to the effect of the UV background. The potential of these processes to bring the abundance of Milky Way–like CDM halos into agreement with observations has already been demonstrated using semianalytical (Benson et al. 2002; Somerville 2001; Font et al. 2011; Guo et al. 2011) and hydrodynamical N-body models (see, e.g., Nickerson et al. 2011; Shen et al. 2014; Wheeler et al. 2015; Sawala et al. 2016). The results of our SAM for the CDM case (see Figure 3, top left panel) confirm that the strong feedback adopted for the CDM model (Section 2.3) can bring the predicted abundance of low-mass luminous satellites close to the observed value. Specifically, we considered the predicted stellar mass function of Milky Way–like halos, selected as those with DM mass in the range $M = 1–2.5 \cdot 10^{12} M_\odot$ (where M is the mass of a spherical volume with mean density equal to 200 times the critical density), which covers the bulk of the observational
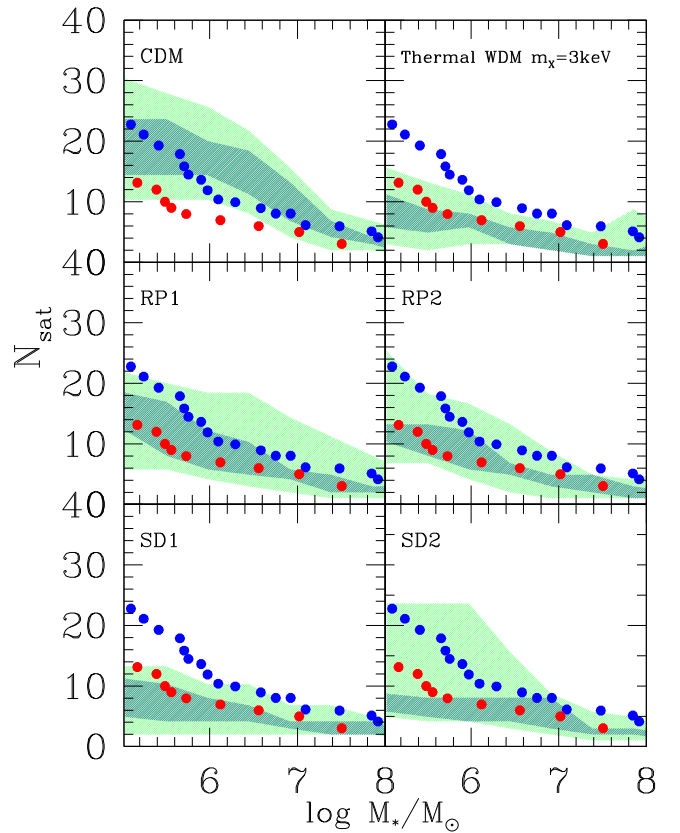

Figure 3. Stellar mass functions of satellites of Milky Way–like galaxies in the models are represented as shaded regions enclosing 68% (darker) and 95% (lighter) of the satellites of halos with DM mass in the range $M = (1–2.5) \cdot 10^{12} M_\odot$. These are compared with the compilation of observational data by McConnachie (2012) for the Milky Way satellites (red dots) and for the satellites of M31 (blue dots).

estimates of the Milky Way mass (for a comprehensive account of such measurements, see Wang et al. 2015). For the CDM case, we find that the predicted stellar mass function deviates by less than 1σ from the observed stellar mass function of M31, while still slightly overestimating the observed abundances of Milky Way satellites. The latter, however, should be considered as an effective lower limit due to the limited sky coverage of local galaxy surveys and the low surface brightness of dwarf galaxies (while the satellite counts of M31 should be closer to completeness for $M_* \geqslant 10^5 M_\odot$).

The observed abundance of satellites provides an indication of a tension with the predictions of the thermal $m_X = 3$ keV WDM model and of the SD1 model, which underestimate the observed numbers. These indeed are the models characterized by a stronger suppression of the power spectrum compared to CDM (see Figure 1); in the case of the thermal WDM model with $m_X = 3$ keV, such a conclusion agrees with what was found by Kennedy et al. (2014). As for the RP scenario, our RP1 and RP2 models are close to the LA8 and LA12 models explored by Lovell et al. (2017b), corresponding to RP models with $m_\nu = 7$ keV and lepton asymmetry $L_6 = 8$ and $L_6 = 12$, respectively. For such models, we find consistent results, since both RP1 and RP2 match the observed satellite distributions obtained by Lovell et al. (2017b) for the LA8 and LA12 models. The convergence of our results with existing works on the impact of RP models on the Milky Way satellites is

encouraging and supports the robustness of our conclusions. Indeed, we have verified that such conclusions are not changed when more elaborate scaling laws for the supernova feedback (like the evolving feedback model in Hou et al. 2016) are assumed, or when the assumed value for $z_{\rm cut}$ (Section 2.3) is varied in the range $z_{\rm cut} = 7$–10.

In principle, the degeneracy between feedback effects and the effects of assuming DM models with suppressed power spectra affecting the comparison with the stellar mass function of satellite galaxies could be broken by investigating the stellar-to-halo mass ratios predicted by the different DM models. In fact, we expect the strong feedback needed in CDM to match the observed shape of the stellar mass distributions to yield lower M_*/M ratios at small mass scales compared to the WDM and SN DM models. However, while M_*/M ratios constitute a straightforward prediction of the models, on the observational side, the measurements of the DM mass M are subject to several uncertainties and biases. In fact, these are usually based on observed rotation velocities $v_{\rm rot}$ measured through H I widths. However, the latter are related to the maximum circular velocity of the dark matter halo $v_{\rm max}$ (and hence to M) by relations depending on the assumed density profile, which in turn depends on the assumed cosmology and on the feedback effects. While high-resolution hydrodynamical simulations suggest a strong deviation of $v_{\rm rot}$ from $v_{\rm max}$ due to strong stellar feedback (see, e.g., Macció et al. 2016; Brooks et al. 2017), which provides shallower density distributions compared to the NFW form, observationally based estimates from H I rotation curves indicate a smaller difference (Papastergis & Shankar 2016; Trujillo-Gomez et al. 2016; Read et al. 2017). Further uncertainties are introduced by the subtle procedure to obtain an inclination-corrected H I profile half-width from the observed line-of-sight rotation velocities (see, e.g., Papastergis et al. 2015).

Such a complex observational situation strongly affects the comparison with models, shown in Figure 4. To account for the uncertainties and biases affecting the observational determination of M, we compare the predictions of our DM models with the measurements from different groups that adopted different strategies. Ferrero et al. (2012) use H I rotation curves and stellar masses of galaxies compiled from the literature and use the outermost point of the rotation curve as a (conservative) proxy for $v_{\rm max}$; in the cases of galaxies with peculiar rotation curves, they use the velocity of the maximum of the rotation curve. Read et al. (2017) fit fully resolved H I rotation curves of individual field dwarfs, allowing for both an NFW profile and for parameterized cored profiles (accounting for baryon-induced cores), and they apply the best-fitting density profile to derive the DM halo mass M. Brook & Di Cintio (2015) convert the observed stellar kinematics of 40 Local Group galaxies to M using the mass-dependent density profile derived from hydrodynamical simulations (Di Cintio et al. 2014), characterized by strong feedback effects; while not affected by issues related to the H I rotation curves, stellar kinematics only probe the very inner region of halos, which are subject to large uncertainties in the halo mass estimates.

We consider the above observational derivations of the M_*/M ratio as representative of the different approaches used in the literature. For example, Pace (2016) base their work on Little THINGS and THINGS rotation curves fitted with the Di Cintio et al. (2014) halo profile. For larger halos, Katz et al. (2017) use 147 rotation curves from the SPARC sample.

Schneider et al. (2017a) follow a different approach to derive the DM mass. They select a sample of 109 galaxies from the catalog by Papastergis & Shankar (2016) with rotation velocities measured to radii larger than three galactic half-light radius. This additional selection criterion guarantees that the velocity measurement is not dominated by baryonic effects. In addition, they allow for cored profiles analogously to Read et al. (2017).

We find that the strong supernovae feedback required by the CDM model to match the observed flat faint-end logarithmic slope of the stellar mass distributions yields a low M_*/M ratio at the scale of dwarf galaxies: at mass scales $M \lesssim 10^9 M_\odot$, we obtain $M_*/M \leqslant 10^{-5}$. This is a well-known feature of CDM models, as shown, for example, by the blue line in Figure 4 representing the average ratios found by the full SAM model by Guo et al. (2011) applied to large cosmological N-body simulations in the CDM case. A similar trend for CDM has been found using abundance-matching techniques (Guo et al. 2010; Moster et al. 2010; Behroozi et al. 2013) or hydrodynamical simulations (Macció et al. 2016). Note that scatter in the predicted (M_*/M)–M relation increases dramatically for decreasing masses $M \lesssim 10^9 M_\odot$. Indeed, at the faintest end of the distribution, a galaxy cannot be assigned a unique halo mass based solely on its stellar mass. Such a result is consistent with what was found in recent N-body simulations (see Munshi et al. 2017).

A different behavior characterizes the predictions from WDM and SN models. In these cases, M_*/M ratios in the whole range $10^{-5} \lesssim M_*/M \lesssim 10^{-2}$ are found for low-mass halos $M \lesssim 10^9 M_\odot$. This is because the suppression in the DM power spectrum at such mass scales allows us to match the observed stellar mass distributions with a milder feedback (see Section 2.1), thus yielding larger M_*/M ratios, an effect pointed out—for the thermal WDM case—in earlier works (see, e.g., Papastergis et al. 2015). While, in principle, the comparison of model predictions with the observed (M_*/M)–M relation could constitute a sensitive probe for the DM scenarios, with the present data distribution better matched by WDM and SN models, the uncertainties outlined above result in data that are too sparse to support any strong conclusions. Upcoming large-area H I surveys with interferometric data, allowing for a detailed sampling of the rotational curves of low-mass galaxies, will greatly improve the observational situation in the next few years.

3.2. Evolution

We now turn to investigating how assuming DM models based on SN affects the evolution of the galaxy population. We start by comparing the evolution of the stellar mass function predicted by the considered SN models with the observed distributions (Figure 5). In this case, we do not find any significant effect in the considered stellar mass range. Such results are consistent with recent findings obtained from SAMs coupled to high-resolution simulations for thermal WDM with $m_X = 1.5$ keV (Wang et al. 2017). This is not unexpected, since the range of stellar masses $M_* \gtrsim 10^8 M_\odot$ probed by the observations corresponds to DM halos $M \gtrsim 10^9 M_\odot$, too large to be appreciably affected by the WDM and SN models considered here, characterized by half-mode masses $M \lesssim 10^9 M_\odot$ (although the observed range of stellar masses could probe WDM models with smaller values of $m_X \lesssim 1$ keV, corresponding to $M_{1/2} \approx 10^{10} M_\odot$, as shown in Menci et al.
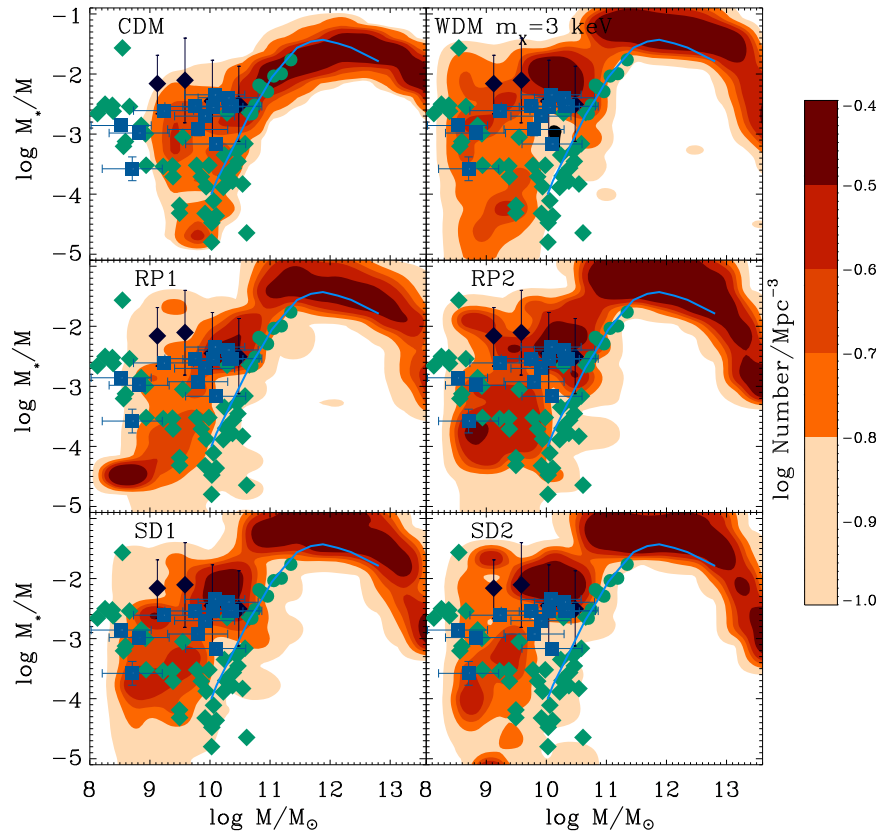
Figure 4. Stellar-to-halo mass ratios M_*/M as a function of the halo mass M of model galaxies are shown as colored contours for the different assumed DM models. These are compared with different sets of data from Ferrero et al. (2012, black points), Brook & Di Cintio (2015, green points), and Read et al. (2017, blue squares). For the latter, we excluded the Leo T data where no rotation curves are available. The blue line is the average relation obtained for CDM by Guo et al. (2011) using a semianalytic model applied to large, cosmological N-body simulations.

2012). Pushing the comparison to smaller stellar masses $M_* \leqslant 10^9\,M_\odot$ constitutes a challenging task even in the near future, since at such masses (and especially at high redshifts) the derivation of the observed stellar mass is affected by corrections to account for the Eddington bias, which are not trivial to compute (see Grazian et al. 2015; Davidzon et al. 2017 for details).

A radically different situation holds when we compare with the observed UV luminosity functions up to very high redshifts $z = 6$ (Figure 6). In fact, the gravitational lensing magnification of background galaxies provided by foreground clusters has been recently exploited in the framework of the Hubble Frontier Field (HFF) program, leading to the measurement of the UV luminosity function down to extremely faint magnitudes $M_{UV} \approx -12$ at high redshifts $6 \leqslant z \leqslant 8$ (Livermore et al. 2017). Indeed, comparing the measured abundance of the faintest galaxies with the maximum number density of DM halos in WDM cosmologies has already allowed us to set a robust limit $m_X \geqslant 2.4$ keV independently of baryon physics for the mass of thermal relic WDM particles at the 2σ confidence level (Menci et al. 2016) and to effectively constrain the parameter space of SN models (Menci et al. 2017). The above limits are very conservative, since they are derived by comparing the observed number density of galaxies with the *maximum* abundance of halos in different DM models; we thus expect that tighter constraints can be obtained when the observed abundances are compared with the number density of luminous ($M_{UV} \lesssim -12$) galaxies predicted by different DM models. Such a comparison is performed in detail in Figure 6,

where the UV luminosity functions of galaxies are compared with existing observations up to $z = 6$.

For the CDM case, we recover the long-standing problem of the overproduction of low-luminosity galaxies at redshift 2–4 (see, e.g., Somerville et al. 2001; Croton et al. 2006; Lo Faro et al. 2009; Gruppioni et al. 2015), an instance of the CDM small-scale issues. On the other hand, the lower abundance of low-mass galaxies characterizing models with suppressed power spectra provides a better fit to the UV luminosity functions up to redshift $z \approx 4$ (as already noted in Menci et al. 2012 for the thermal WDM case), but compares critically with the observed abundance at $z \approx 6$. This is indeed the most effective probe for the abundance of early-forming, low-mass galaxies and, hence, for the effects of suppressed power spectra. However, although the number density derived by Livermore et al. (2017) is robust from the statistical point of view, there could be subtle systematic effects related to the estimation of the survey volume, that is, the variance of the lensing magnification maps of HFF clusters and the physical sizes of faint, high-z galaxies (which enter the completeness correction). These have been claimed to affect the number density of high-redshift galaxies in the faintest bins, potentially leading to a flatter slope of the UV luminosity function at the faint end (Bouwens et al. 2017a, 2017b; see also Kawamata et al. 2017). Thus, the conservative estimation of the UV luminosity function of Bouwens et al. (2017b) has also been shown in Figure 6, to provide an overview of the present observational situation.
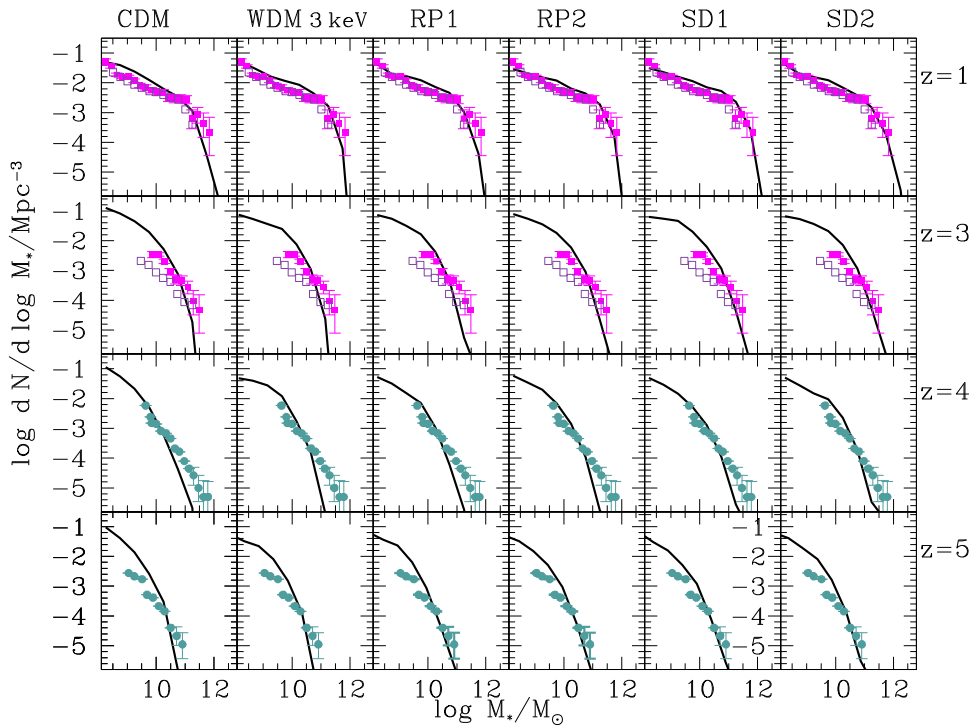
Figure 5. Evolution of the predicted stellar mass function for the different DM models considered in the text and indicated at the top of the plot; the different redshifts are indicated on the right. Data for $z \leqslant 3$ are taken from Santini et al. (2012, solid squares) and Tomczak et al. (2014, open squares), while for $z \geqslant 4$, data are taken from Grazian et al. (2015).

We obtain that all models with suppressed spectra underestimate the abundance of high-z galaxies with $M_{\mathrm{UV}} \gtrsim -14$ measured by Livermore et al. (2017); the two DM models with the most suppressed spectra (the thermal WDM case with $m_X = 3$ keV and the SD1 model) also underestimate the more conservative observational estimates (Bouwens et al. 2017b) of the abundance of $z = 6$ faint galaxies, with a discrepancy $\gtrsim 1\sigma$. When models are compared with the Livermore et al. (2017) measurements, the WDM case with $m_X = 3$ keV and the SD1 model underestimate the observed abundances by more than 2σ, while the RP1, RP2, and SD2 models deviate by $\approx 1 - \sigma$. This shows that at present the UV luminosity functions at high z constitute an extremely powerful probe for the DM scenarios. Thus, on the observational side, the first step to improve the results presented in this paper consists in a deeper understanding of the systematics associated with the lensing observations of faint, high-redshift galaxies. In fact, the analysis of the HFF observations is open to several advancements (see, e.g., Castellano et al. 2016). In addition, the present measurements of the UV luminosity functions from the HFF are based only on the first two fields of the HFF survey: the inclusion of the remaining four strong lensing clusters (Lotz et al. 2017) will reduce both statistical uncertainties and mitigate possible cosmic variance effects. In a few years, a significant leap will be made possible by the availability of deep *JWST* imaging. In particular, the capability of reaching 30.5 AB (at S/N = 5) in deep NIRCam fields (e.g., Finkelstein et al. 2015a, 2015c) will improve by 1.5 mag the depth of current HFF imaging, reaching absolute magnitudes of $M_{\mathrm{UV}} \approx -11$, and will yield five times larger samples of high-redshift galaxies (Laporte et al. 2015) while significantly improving photometric selections through the availability of rest-frame optical photometry of high-z sources.

3.3. Star Formation

Finally, we investigate the star formation properties of the galaxy populations in the different DM models considered here. In Figure 7 we plot the global SFR densities from our models and compare them with the observed values. The observational values have been taken from the review paper by Madau & Dikinson (2014), who collected a large set of measurements in the literature, obtained either from UV or from far-IR rest-frame observations (see caption). To perform a proper comparison, the model star formation densities have been obtained including all galaxies brighter than $0.03 \, L_*$, the same threshold adopted for the observational values. All of the models yield SFR densities consistent with observations. This is mainly because in the star formation density $\psi = \int N(\dot{M}_*)\dot{M}_* \, d\dot{M}_*$ the number density $N(\dot{M}_*)$ of galaxies is weighted with the SFR $\dot{M}_*$. While the first is suppressed for low-mass galaxies in all DM models with a suppressed power spectrum, such an effect is balanced by the larger $\dot{M}_*$ associated with these galaxies in such models due to the smaller adopted feedback efficiency (see Section 2). Such a result shows that the star formation density does not constitute an effective probe for the different DM scenarios, since in this case the DM and the baryonic effects are highly degenerate, at least in the luminosity range ($L^* \geqslant 0.03 \, L_*$) explored by the present measurements.

However, a deeper insight can be gained by investigating the star formation histories of low-mass galaxies in the different scenarios. In Figure 8 we show the stellar mass growth histories of low-mass galaxies for all of the considered DM models. This is defined as the stellar mass formed in all progenitors of a given galaxy by a given cosmic time t normalized to the stellar mass of the galaxy at $z = 0$. In the figure, we consider only
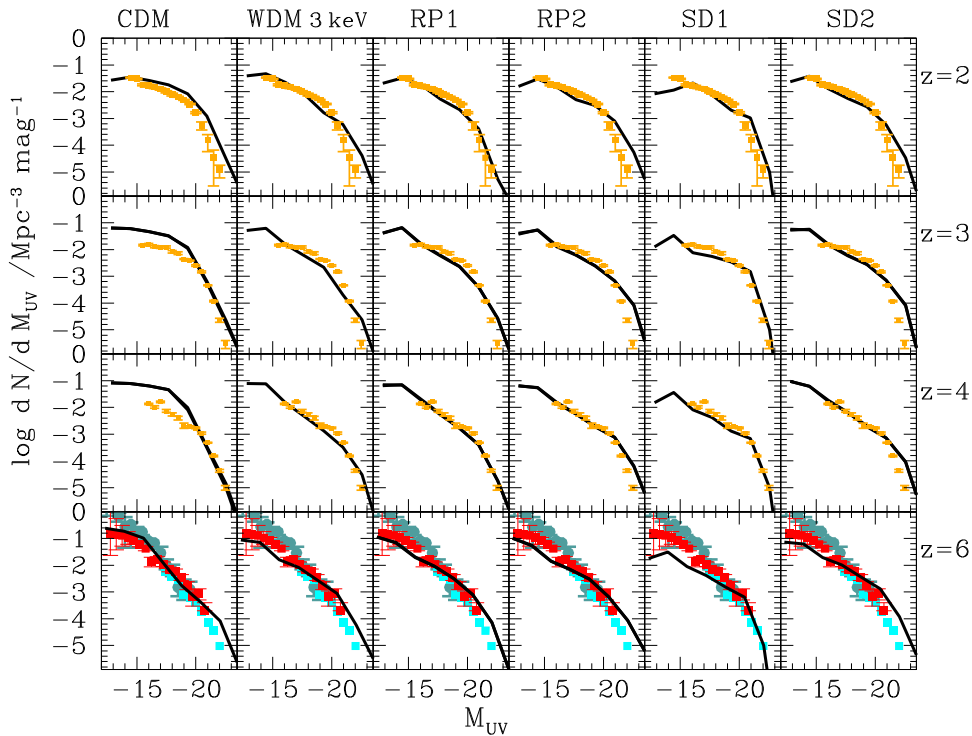
Figure 6. Evolution of the predicted UV luminosity function for the different DM models considered in the text and indicated at the top of the plot; the different redshifts are indicated on the right. Data for $z \leqslant 4$ are taken from Parsa et al. (2016). Data in the highest redshift bin are taken from Livermore et al. (2017, dark green circles) and from Bouwens et al. (2017b, red squares) for the faint end, while for the bright end we compare with Finkelstein et al. (2015c, light cyan squares).
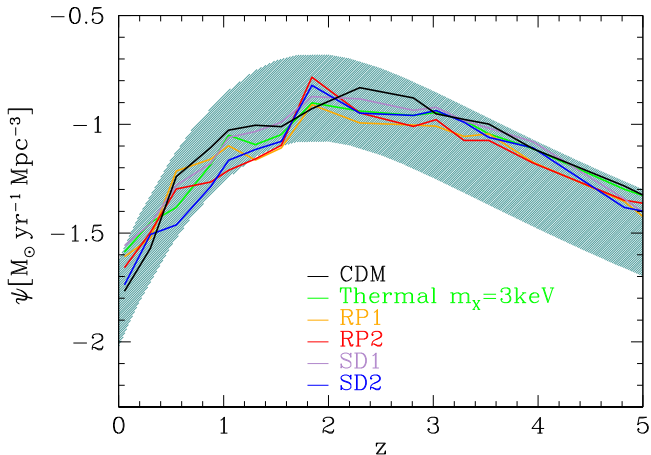
Figure 7. Predicted star formation rate density for the different DM models considered in the text, shown by the labels. The shaded region corresponds to the present uncertainties as a result of the compilation of data in Madau & Dickinson (2014), who consider only surveys that have measured SFRs from rest-frame far-UV (generally 1500A), mid-IR, or far-IR measurements, and including all galaxies with luminosities larger than 0.03 L_*, where L_* is the characteristic luminosity of the considered data sample. For the model predictions, we adopted the same lower luminosity cut, deriving L^* as the ratio between the second and the first moment of the UV luminosity functions.

low-mass galaxies (stellar masses $9 \leqslant \log M_*/M_\odot \leqslant 9.5$ at $z = 0$), the ones affected by the assumed DM power spectrum. The large suppression in the number of progenitors of low-mass galaxies occurring in models with a suppressed power spectrum overwhelms the larger star formation occurring in each progenitor due to milder feedback, and leads to an overall delay in the growth of the stellar mass component of dwarf galaxies. The effective delay depends on the assumed DM scenario. Taking as a reference value the time at which 80% of

the final stellar mass is formed in the progenitors (shown by the dashed lines in the figure), we obtain delays ranging from $\sim$1 Gyr (in the case of thermal WDM) to $\sim$500 Myr. Our findings are consistent with existing results in the literature obtained for the WDM case. For example, in the hydrodynamical simulations by Governato et al. (2015), a delay $\sim$0.5–1 Gyr is found when comparing the stellar growth of a thermal WDM model with $m_X = 2$ keV with the CDM predictions.

Such an effect is particularly interesting, since it allows for observational tests of the DM scenarios using different indicators of the build-up of the stellar component in dwarf galaxies. An instance is provided by the specific star formation rate (SSFR), defined as SSFR $\equiv \dot{M}_*/M_*$. It is a measure of the present star formation activity normalized to the total number of stars formed during the past history of star formation and mass assembly. In particular, values much smaller than the inverse of the Hubble time (typically $0.3/t_H \approx 0.2 \times 10^{-10}$; see, e.g., Damen et al. 2009) correspond to quiescent galaxies, which must have formed most of their stellar mass at earlier times. Observational estimates of the full SSFR distributions based on the large statistics provided by the SDSS catalog have been obtained by several authors (see, e.g., Balogh et al. 2004; McGee et al. 2011; Peng et al. 2012; Wetzel et al. 2012). Here (Figure 9) we compare with the distributions obtained by Wetzel et al. (2013) based on the spectroscopic NYU Value-Added Galaxy Catalog (NYU-VAGC; Blanton et al. 2005) from SDSS data release 7 (Abazajian et al. 2009), who constructed stellar mass limited samples complete down to stellar masses $M_* = 5 \times 10^9 M_\odot$ and magnitudes $M_r = -19$. The measured SSFRs are based on the spectral reductions by Brichmann et al. (2004) with updated prescriptions for AGN contamination and are derived from emission lines for SSFR $\geqslant 10^{-11}$ yr^{-1} and from a combination of emission lines
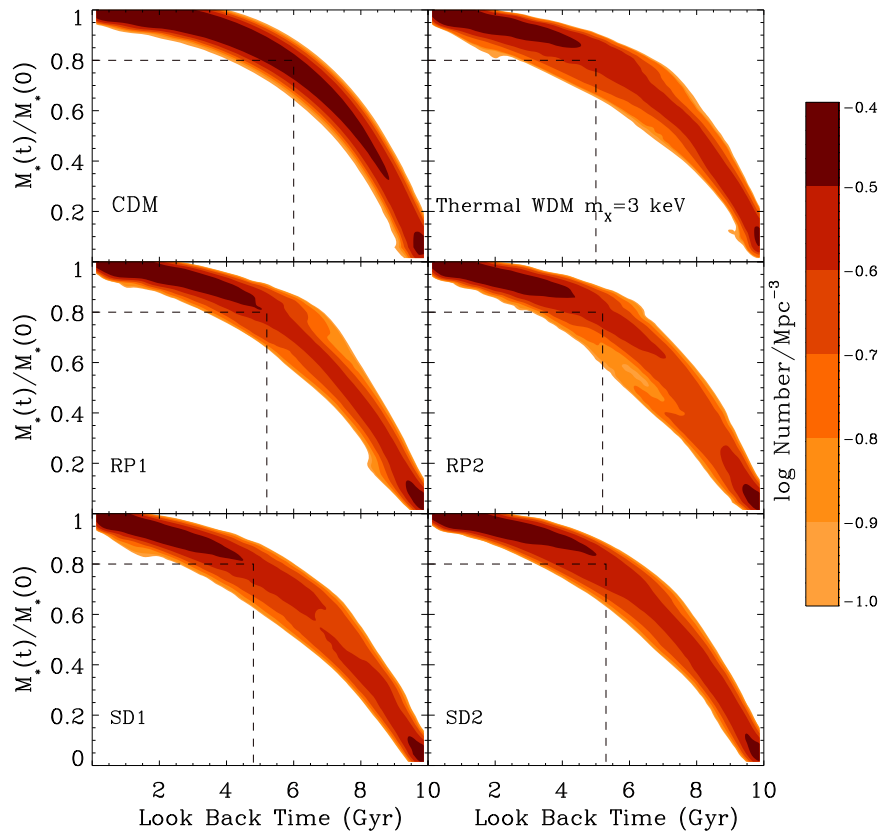
Figure 8. Predicted stellar growth histories for the DM models indicated by the labels. The contours show, at given look-back time, the number of model galaxies with a given ratio $M_*(t)/M_*(0)$ between the mass formed in all progenitors of the final galaxies and the final stellar mass. Only galaxies with final mass $9 \leqslant \log M_*/M_\odot \leqslant 9.5$ are considered. The dashed line shows the look-back time corresponding to the formation of 80% of the final stellar mass.

and $D_n 4000$ for lower values of the SSFR. In the above sample of galaxies, Wetzel et al. (2013) have identified the objects that occupy the same host halo through a modified implementation of the group-finding algorithm of Yang et al. (2005, 2007); this allowed them to obtain separate SSFR distributions for central and satellite galaxies (see Wetzel et al. 2013).

The above observational distributions are compared with our predictions for the different DM models in Figure 9. To comply with the procedure adopted for observational distributions, model galaxies with log SSFR/yr$^{-1} \leqslant -12$ have been assigned a random Gaussian value centered at log SSFR/yr$^{-1} = -0.3 \log(M^*/M_\odot) - 8.6$ and dispersion 0.5. A clear bimodal distribution is found, in agreement with previous results from SAMs based on simulations (Guo et al. 2011, Henriques et al. 2015). The detailed balance between passive and active galaxies and between environmental and internal quenching depends on the details of the implemented baryonic processes, including time-dependent strangulation effects (e.g., Guo et al. 2011), which we do not consider in this work. However, we find a systematic increase in the star-forming fraction of low-mass galaxies when models with suppressed power spectra are considered (in the first two rows, the strongest peaks at log SSFR/yr$^{-1} \approx -10$ are present in columns 2–6 when compared to the first column). Such an effect cannot originate only from environmental quenching processes affecting satellites since, to some extent, they are also present in central galaxies. Thus, it must originate from the delays in the star formation histories of models with suppressed power spectra compared to CDM shown in Figure 9. In such models, the stellar mass growth histories are

skewed toward later cosmic times, yielding a larger fraction of active galaxies (with SSFR $\geqslant 10^{-11}$ yr^{-1}) compared to the CDM case.

A useful diagnostic to probe the above effects of the adopted DM power spectrum on the star formation histories of galaxies is the cumulative age distribution of stellar populations in local galaxies. The importance of this topic was already shown in the work of Calura et al. (2008), where they compared the age distribution of galaxies calculated in an SAM assuming a CDM cosmology to those computed within a WDM model, assuming that the WDM was constituted by thermal relic particles of mass 0.75 keV.

In Figure 10 we show the observed cumulative age distributions of SDSS galaxies, which were first presented in Gallazzi et al. (2008), compared to the theoretical distributions computed assuming different DM scenarios. As explained in Calura et al. (2014), for the purpose of a fairer comparison between observations and models, the mass-weighted ages of the stellar populations in local galaxies were recalculated to weight each galaxy spectrum by $1/V_{max}$, where V_{max} is defined as the maximum visibility volume given by the bright and faint magnitude limits of the observational data set, $14.5 \leqslant r \leqslant 17.77$.

The steeper rise of the CDM age distribution reflects the extreme paucity of young galaxies characterizing this model. All of the models computed in the alternative cosmologies show a similar behavior and a better agreement with the observed distribution than the CDM model. In general, even if the percentage of young galaxies is underestimated by all models, the striking feature is that all of the models with
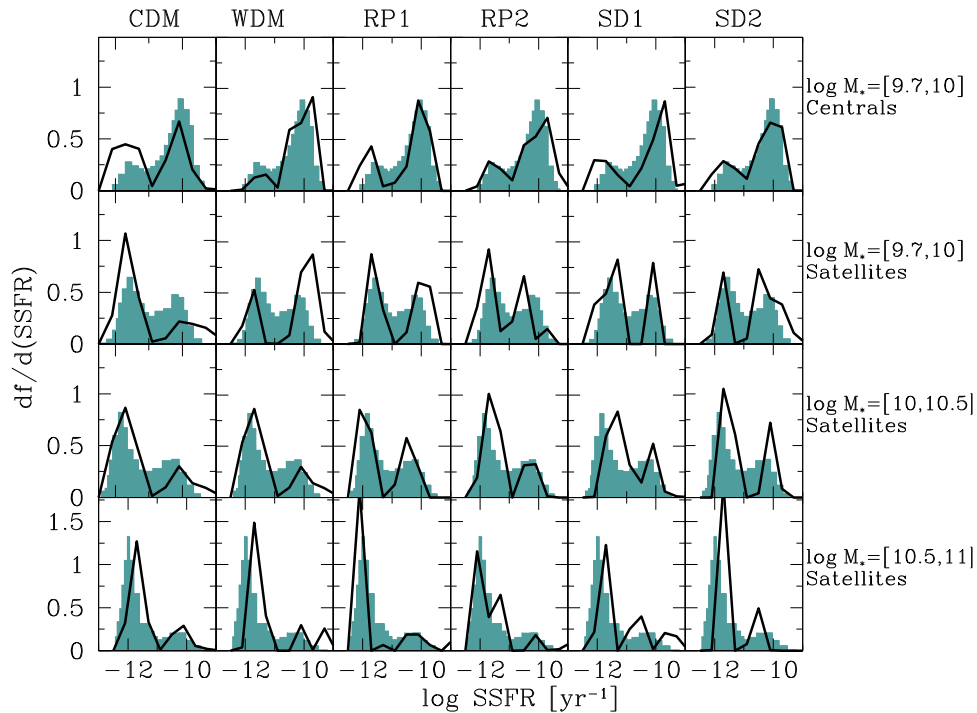
Figure 9. Predicted distributions of specific star formation rate (solid lines) for central and satellite galaxies in different mass bins as indicated by the labels, for the different DM models indicated on the top. The solid histograms are the observed distributions measured by Wetzel et al. (2013).
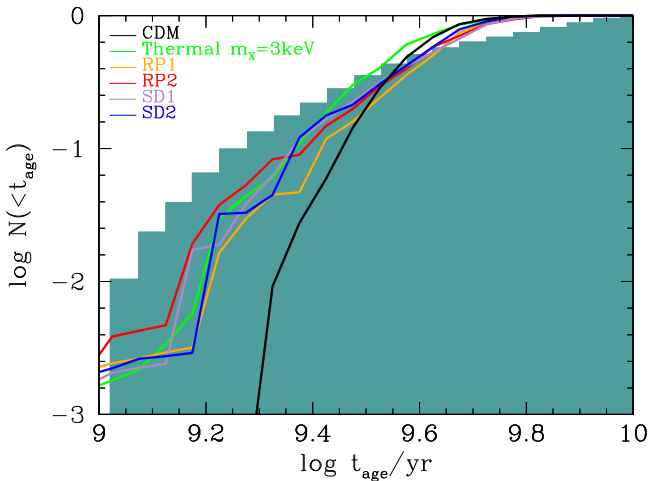

Figure 10. For the different DM scenarios considered in the text, we plot the predicted cumulative distributions of the mass-weighted age t_{age} for the different DM models (solid lines) and compare them with the data by Gallazzi et al. (2008, solid histogram) weighted as described in Calura et al. (2014; see the text). In the plot we have considered all galaxies with $M \geqslant 10^9 M_\odot$.

suppressed power spectra show the presence of galaxies younger than $10^{9.3}$ years, absent in the CDM model. Such a result is qualitatively in agreement with that obtained by Calura et al. (2014), although in that work the assumed WDM power spectra were much more extreme and chosen in order to underline the differences with the CDM scenario. In the future, it will be interesting to study how the ages of the stellar populations of local galaxies are distributed as a function of the stellar mass in all of the different cosmological models considered in this work: this very aspect will be addressed in a forthcoming work.

The enhanced presence of young, low-mass galaxies in the DM models with suppressed power spectra compared to the

CDM case can be further investigated by studying the integrated photometric properties of galaxies.

In the past, the integrated colors of composite stellar populations turned out to be extremely useful in gaining crucial clues on their formation history, as shown in previous works addressing the star formation history of dwarf spheroidal galaxies (dSph) and dwarf irregulars in the Local Group (Mateo 1998), a possible evolutionary connection between these two classes (e.g., Skillman & Bender 1995), as well as the link of dSphs with large spheroids (Calura et al. 2008).

In Figure 11 we show the distribution of $(U - B)$ colors, plotted as a function of the absolute B-band magnitude, as computed by means of our SAM assuming different cosmologies and compared to an observational sample drawn from the SDSS data set (Data Release 14). Here we focus mostly on the faintest systems, since, as already discussed, the major differences between CDM and WDM/SN spectra concern mass scales $M \lesssim 10^9 M_\odot$, that is, halos that presumably host faint, dwarf galaxies. Thus, we have extracted from the entire SDSS sample of local ($z < 0.1$) galaxies only those with stellar masses $M_* \leqslant 10^{9.5} M_\odot$.[4]

The large fraction of young, star-forming dwarf galaxies obtained in DM models with suppressed spectra shows up in the distribution of galaxies in the color–magnitude plane. In fact, the $U - B$ color constitutes a proxy for the SSFR of galaxies (although it is also affected by dust extinction). The bimodality in the SSFR distributions discussed above is reflected here in two classes of galaxies: the ones with bluer colors, mainly contributed by low-luminosity objects, constituting the "blue cloud," and the "red sequence" characterized by red colors $(U - B) \geqslant 1$, mainly contributed by brighter objects. The distribution of observed points thus defines the

---

[4] For the SDSS galaxies, the stellar masses have been calculated using the Bruzual & Charlot (2003) stellar population synthesis models.
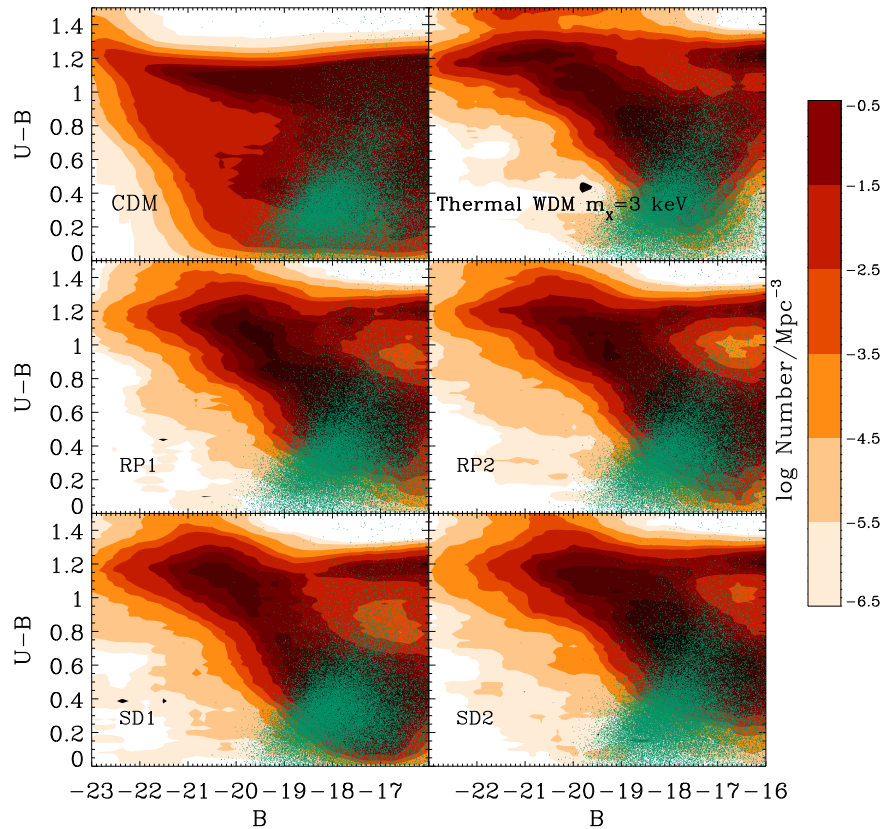
Figure 11. For the different DM scenarios considered in the text, we show as a contour plot the distribution of model galaxies for $z \leqslant 0.1$ in the color–magnitude plane, $U - B$ vs. B (Vega magnitudes). These are compared with the data from the SDSS for dwarf galaxies with $M_* \leqslant 10^{9.5}\,M_\odot$ (green points; SDSS magnitudes have been converted using the relations in Fukugita et al. 1996). We included only galaxies brighter than the completeness limit $g = 22.2$ of the SDSS survey at $z = 0.1$.

position and the relative population of the dwarf galaxies belonging to the blue cloud.

Although all of the DM models yield a bimodal distribution in the color–magnitude plane, the WDM and SN models present a more pronounced correlation between color and B-band magnitude (see, e.g., Faber et al. 2007; Pierce et al. 2010) compared with the CDM predictions.

At the faintest magnitudes ($B \geqslant -19$), the theoretical color distributions computed assuming different DM scenarios show the most marked differences. In particular, at these magnitudes, the CDM model predicts that a major fraction of galaxies have red colors ($U - B$) > 0.8, whereas observations indicate that faint galaxies populate preferentially the region with ($U - B$) ≈ 0.3–0.4 (a long-standing problem of CDM scenarios; see Kimm et al. 2009; Davé et al. 2011; Bower et al. 2012; Hirschmann et al. 2012, 2013; Weinmann et al. 2012). On the other hand, in all models with suppressed power spectra, the maximum density of faint systems is generally visible at colors ($U - B$) < 0.7, in better agreement with the observational data, which are particularly crowded at $B \approx -18$ and ($U - B$) ≈ 0.3–0.4. Among the considered models, the one that best reproduces the data is SN SD1, which shows a remarkable overlap of the position of its densest region and the one of the observational distribution.

Such a striking difference in the predictions of CDM and the WDM and SN models, which concerns the abundance of blue, faint galaxies, is due to the combined effects of the strong feedback adopted in the CDM model (required to comply with the flat slope of the local stellar mass functions) and of the

delayed star formation histories characterizing the WDM and SN models. In the future, in order to gain more clues on the nature of DM and to further probe the DM models, more observables will need to be investigated, possibly sensitive to the presence of young stellar populations in dwarf galaxies in particular. These observables may include, for example, the gas-to-stellar mass fractions or the cold gas content in general of such systems, as well as their star formation history, generally addressable by means of color–magnitude diagrams (e.g., Sacchi et al. 2016; Vincenzo et al. 2016).

4. Summary and Conclusions

We have used a SAM to investigate galaxy formation in cosmological models with dark matter constituted by sterile neutrinos. We focused on models with fixed sterile neutrino mass $m_\nu = 7\,\mathrm{keV}$, consistent with the tentative $3.5\,\mathrm{keV}$ line recently detected in several X-ray spectra of clusters and galaxies. Specifically, we chose to focus on SN models that are marginally consistent with existing bounds but still yielding an appreciable suppression of the power spectrum with respect to CDM at scales $M \lesssim 10^9\,M_\odot$. In particular, we considered the following:

1. Two resonant production models of sterile neutrinos with mixing angles $\sin^2(2\theta) = 2 \times 10^{-10}$ (model RP1) and $\sin^2(2\theta) = 5 \times 10^{-11}$ (model RP2), to cover the range of mixing parameters that is consistent with the tentative $3.5\,\mathrm{keV}$ line.

2. Two scalar-decay models representative of the two possible cases characterizing such a scenario, a freeze-in (model SD1) and a freeze-out case (model SD2), both with coupling parameter $10^{-8.5}$ between the scalar and the sterile neutrino fields, but with different coupling of the scalar with the Higgs field.

3. For comparison, we also considered the standard CDM case and the thermal WDM with particle mass $m_X = 3$ keV.

Following the approach of previous works on the comparison between CDM and WDM (e.g., Kennedy et al. 2014; Wang et al. 2017), we calibrated the feedback parameter of our SAM to match the shape of the local stellar mass distribution, and we investigated the effects of assuming the different DM models on the model predictions, comparing the result of our SAM to a wide set of observables. The aim is to investigate to what extent the comparison with the different observables can help to disentangle the effects of baryon physics (in particular of feedback) from the specific effects of the different assumed DM models, so as to single out the most promising observational probes for the DM scenario driving galaxy formation. We found the following:

1. The stellar mass function of satellites of Milky Way–like galaxies is prone to the degeneracy between the effects of feedback and those related to the DM power spectrum. These are both effective in yielding satellite abundances consistent with recent observations. Nevertheless, the predictions of both the thermal WDM and the SD1 models are in tension with the present data since the corresponding predicted abundances are below (at more than 1σ c.l.) the observed data.

2. Measurements of the stellar-to-halo mass ratios in low-mass galaxies constitute in principle an effective way to disentangle the effects of feedback from those related to the DM power spectrum. All of the considered DM models yield a large fraction of dwarf galaxies with $-4 \leqslant \log(M_*/M) \leqslant -2$ for $M \leqslant 10^9 M_\odot$, at variance with the CDM scenario. However, the present data are too sparse (due to the observational biases discussed in Section 3) to provide definite evidence for such ratios.

3. The abundance of faint ($M_{\mathrm{UV}} \geqslant -12.5$) galaxies in the UV luminosity functions at redshifts $z \geqslant 6$ constitutes at present the most clean way to probe DM scenarios based on WDM or on sterile neutrinos. Even maximizing the systematic effects affecting present observations (see Bouwens 2017a, 2017b; Kawamata et al. 2017), the SD1 model is excluded at the greater than 1σ confidence level. In the future, improvements in the measurements of the faint end of the UV luminosity function will provide a powerful probe for DM models based on SNs.

4. The star formation properties of dwarf galaxies (stellar masses $M_* \sim 10^9 M_\odot$) depend on the assumed DM model; DM models with suppressed power spectra are characterized by a delay in the stellar mass growth history ranging from 500 Myr (RP1 and SD2 models) to $\approx$1 Gyr. This yields for such models a larger fraction of active (SSFR $\geqslant 10^{-11}$ yr^{-1}) galaxies with blue colors ($U - B \leqslant 1$) and young age ($\leqslant 10^9$ years) compared to the CDM case, providing a better match to the present data. Such conclusions are robust with respect to the variation in the feedback efficiency *when* the latter is calibrated in each model so as to match the slope of the local stellar mass function.

The comparison with existing works on galaxy formation in thermal WDM models (and in SN DM models, when comparing with the Milky Way satellites) supports the sensibleness of our approach and the robustness of our results. Indeed, our strategy for fixing the feedback parameters follows that adopted in recent works based on SAM (see, e.g., Kennedy et al. 2014, Lovell et al. 2016; Wang et al. 2017). For the abundance of satellite galaxies in the thermal WDM case (with $m_X = 3$ keV), we recover the tension between the predicted and the observed values found in Kennedy et al. (2014) for our assumed value of the mass of Milky Way–like galaxies ($M = (1-2.5) \cdot 10^{12} M_\odot$). When we compare our RP1 and RP2 models with the LA8 and LA12 models explored by Lovell et al. (2017a, characterized by similar sterile neutrino mass and mixing parameters), we recover similar results. The larger M_*/M ratios that we find in SN and in the WDM models compared with the CDM case are similar to what were found in previous works (e.g., Guo et al. 2011 for the CDM case, Corasaniti et al. 2017 for the WDM case), while the dramatic increase of the scatter of the M_*/M relation that we find for decreasing masses $M \lesssim 10^9 M_\odot$ is consistent with what was found in recent N-body simulations (see Munshi et al. 2017). The small effect of assuming a WDM spectrum on the shape and evolution of the stellar mass function (with a mild increase in the abundance of high-mass galaxies in models with a suppressed power spectrum) is consistent with the findings in Wang et al. (2017) for their thermal WDM model, while the effects of assuming a WDM power spectrum on the UV luminosity function at high redshift are comparable to what were found by Dayal et al. (2015). Finally, the delay in the growth of the stellar mass in WDM models is quantitatively close to what was found by Governato et al. (2015). Thus, on the theoretical side, our main conclusions fit into the framework that is being outlined by different groups in overlapping cases.

On the observational side, future efforts will soon provide key tools to probe the role of the DM models based on SN in driving galaxy formation. In the near future, the wide survey of the Large Synoptic Survey Telescope (LSST; Ivezic et al. 2016) will cover the whole southern sky at a depth that is around 4 mag deeper than the SDSS: the combination of color information and excess in the surface density of stars will allow significant improvement in the detection of dwarf satellites in the Milky Way and extend it to stellar masses $M_* \sim 10^4 M_\odot$ at a distance of $\sim$1 Mpc. To robustly assess the total masses of these ultrafaint dwarfs, a large leap forward will be provided by dynamical measurements with *JWST*, SKA, and its precursors (ASKAP, MeerKAT, MWA, and HERA). In particular, spectroscopic IFU observations with *JWST* on ultrafaint dwarfs could constrain the dynamical mass of these objects by determining the stellar velocity dispersion or the gas rotation with nebular lines up to large distances from the dwarf center. Particular care, however, should be taken to mitigate the effects of inclination on the dynamical mass estimates and on the role of the environment on the observed ratio of baryonic to total mass. Similarly, SKA and its pathfinders could measure the H I velocity curves of faint galaxies up to large distances from the center, in order to reduce the systematic biases in the total mass estimates. These dynamical mass measurements will allow us to break the present degeneracies between baryonic

feedback and the nature of DM, degeneracies that can still be present when comparing the number statistics of dwarf galaxies (see Figure 4).

As for the abundance of high-z, faint galaxies, our knowledge of the evolution of the UV luminosity function (Figure 7) will be significantly improved by *JWST* observations: NIRCam ultra-deep imaging at $1-5\,\mu$ enables the selection of high-redshift galaxies more than one magnitude fainter than in present *HST* samples (Finkelstein et al. 2015b), extending UV luminosity function estimates both in luminosity and redshift (in principle up to $z \sim 20$). At the same time, *JWST* spectroscopic observations will also tighten constraints on the evolution of the star formation rate density (Figure 7), enabling the measurement of SFR from recombination lines (Hα at $z < 6.5$ and Hβ at higher redshifts) and of dust extinction from the Balmer decrement.

Finally, deep *JWST* observations will greatly improve the reliability of the SSFR, by reducing the associated uncertainties by approximately 0.3 dex of their true value. According to simulations, stellar masses and SFRs will be recovered within 0.2 dex up to $z \sim 9$ (Bisigello et al. 2017) and with higher precision at lower redshifts, thanks to NIRCam multiwavelength imaging and NIRSpec spectroscopic capabilities. With this facility, the observed distribution of SSFRs will be extended toward the range of dwarf galaxies by at least an order of magnitude in stellar mass.

ORCID iDs

N. Menci https://orcid.org/0000-0002-4096-2680
A. Grazian https://orcid.org/0000-0002-5688-0663
F. Calura https://orcid.org/0000-0002-6175-0871
M. Castellano https://orcid.org/0000-0001-9875-8263
P. Santini https://orcid.org/0000-0002-9334-8705

References

Abazajian, K. N. 2014, PhRvL, 112, 161303
Abazajian, K. N., Adelman-McCarthy, J. K., Agüeros, M. A., et al. 2009, ApJS, 182, 543
Ackermann, M., Albert, A., Anderson, B., et al. 2015, PhRvL, 115, 231301
Ade, P. A. R., Aghanim, N., Arnaud, M., et al. 2016, A&A, 594, A13
Adhikari, R., Agostini, M., Ky, N., et al. 2017, JCAP, 01, 025
Adriani, O., Barbarino, G. C., Bazilevskaya, G. A., et al. 2013, PhRvL, 111, 081102
Akerib, D. S., Araújo, H. M., Bai, X., et al. 2014, PhRvL, 112, 091303
Anderson, M. E., Churazov, E., & Bregman, J. N. 2015, MNRAS, 452, 3905
Angulo, R. E., Hahn, O., & Abel, T. 2013, MNRAS, 434, 3337
Aprile, E., Alfonsi, M., Arisaka, K., et al. 2012, PhRvL, 109, 181301
Aprile, E., Arisaka, K., Arneodo, F., et al. 2016, JCAP, 1604, 027
Baldry, I. K., Driver, S. P., Loveday, J., et al. 2012, MNRAS, 421, 621
Balogh, M. L., Baldry, I. K., Nichol, R., et al. 2004, ApJL, 615, L101
Bardeen, J. M., Bond, J. R., Kaiser, N., & Szalay, A. S. 1986, ApJ, 304, 15
Behroozi, P. S., Wechsler, R. H., & Conroy, C. 2013, ApJ, 770, 57
Benson, A. J., Bower, R. G., Frenk, C. S., et al. 2003, ApJ, 599, 38
Benson, A. J., Farahi, A., Cole, S., et al. 2013, MNRAS, 428, 1774
Benson, A. J., Lacey, C. G., Baugh, C. M., Cole, S., & Frenk, C. S. 2002, MNRAS, 333, 156
Bisigello, L., Caputi, K. I., Colina, L., et al. 2017, ApJS, 231, 3
Blanton, M. R., Eisenstein, D., Hogg, D. W., Schlegel, D. J., & Brinkmann, J. 2005, ApJ, 629, 143
Blas, D., Lesgourgues, J., & Tram, T. 2011, JCAP, 1107, 034
Bode, P., Ostriker, J. P., & Turok, N. 2001, ApJ, 556, 93

Bond, J. R., Cole, S., Efstathiou, G., & Kaiser, N. 1991, ApJ, 379, 440
Bose, S., Hellwing, W. A., Frenk, C. S., et al. 2017, MNRAS, 464, 4520
Bouwens, R. J., Illingworth, G. D., Oesch, P. A., et al. 2017a, ApJ, 843, 129
Bouwens, R. J., Oesch, P. A., Illingworth, G. D., Ellis, R. S., & Stefanon, M. 2017b, ApJ, 843, 41
Bower, R. G. 1991, MNRAS, 248, 332
Bower, R. G., Benson, A. J., & Crain, R. A. 2012, MNRAS, 422, 2816
Boyarsky, A., Ruchayskiy, O., Iakubovskyi, D., & Franse, J. 2014, PhRvL, 113, 251301
Boyarsky, A., Ruchayskiy, O., & Shaposhnikov, M. 2009, ARNPS, 59, 191
Brook, C. B., & Di Cintio, A. 2015, MNRAS, 450, 3920
Brooks, A. M., Papastergis, E., Christensen, C. R., et al. 2017, arXiv:1701.07835
Bruzual, G., & Charlot, S. 2003, MNRAS, 344, 1000
Bulbul, E., Markevitch, M., Foster, A., et al. 2014, ApJ, 789, 13
Bulbul, E., Markevitch, M., Foster, A., et al. 2016, ApJ, 831, 55
Bullock, J. S., & Boylan-Kolchin, M. 2017, ARAA, 55, 343
Calura, F., Lanfranchi, G. A., & Matteucci, F. 2008, A&A, 484, 107
Calura, F., Menci, N., & Gallazzi, A. 2014, MNRAS, 440, 2066
Cappelluti, N., Bulbul, E., Foster, A., et al. 2017, arXiv:1701.0793
Castellano, M., Amorin, R., Merlin, E., et al. 2016, A&A, 590A, 31
Cole, S., Lacey, C. G., Baugh, C. M., & Frenk, C. S. 2000, MNRAS, 319, 168
Corasaniti, P. S., Agarwal, S., Marsh, D. J. E., & Das, S. 2017, PhRvD, 95, 3512
Croton, D. J., Springel, V., White, S. D. M., et al. 2006, MNRAS, 365, 11
Damen, M., Labbe, I., Franx, M., et al. 2009, ApJ, 690, 937
Davé, R., Oppenheimer, B. D., & Finlator, K. 2011, MNRAS, 415, 11
Davidzon, I., Ilbert, O., Laigle, C., et al. 2017, A&A, 605, 70
Dayal, P., Mesinger, A., & Pacucci, F. 2015, ApJ, 806, 67
de Vega, H. J., & Sanchez, N. G. 2010, MNRAS, 404, 885
Destri, C., De Vega, P., & Sanchez, N. G. 2013, PhRvD, 88, 3512
Di Cintio, A., Brook, C. B., Dutton, A. A., et al. 2014, MNRAS, 441, 2986
Diemand, J., Kuhlen, M., Madau, P., et al. 2008, Natur, 454, 735
Dodelson, S., & Widrow, L. M. 1994, PhRvL, 72, 17
Efstathiou, G. 1992, MNRAS, 256, 43
Faber, S. M., Willmer, C. N. A., Wolf, C., et al. 2007, ApJ, 665, 265
Ferrero, I., Abadi, M. G., Navarro, J. F., Sales, L. V., & Gurovich, S. 2012, MNRAS, 425, 2817
Finkelstein, S. L., Dunlop, J., Le Fevre, O., & Wilkins, S. 2015a, arXiv:1512.04530
Finkelstein, S. L., Ryan, R. E. J., Papovich, C., et al. 2015b, ApJ, 810, 71
Finkelstein, S. L., Finkelstein, S. L., Finkelstein, S. L., et al. 2015c, ApJ, 810, 71
Font, A. S., Benson, A. J., Bower, R. G., et al. 2011, MNRAS, 417, 1260
Franse, J., Bulbul, E., Foster, A., et al. 2016, ApJ, 829, 124
Fukugita, M., Ichikawa, T., Gunn, J. E., et al. 1996, AJ, 111, 1748
Gallazzi, A., Brinchmann, J., Charlot, S., & White, S. D. M. 2008, MNRAS, 383, 1439
Garrison-Kimmel, S., Boylan-Kolchin, M., Bullock, J. S., & Lee, K. 2014, MNRAS, 438, 2578
Garrison-Kimmel, S., Bullock, J. S., Boylan-Kolchin, M., & Bardwell, E. 2017, MNRAS, 464, 3108
Genzel, R., Tacconi, L. J., Gracia-Carpio, J., et al. 2010, MNRAS, 407, 2091
Ghiglieri, J., & Laine, M. 2015, arXiv:1506.06752
Gonzalez-Perez, V., Lacey, C. G., Baugh, C. M., et al. 2014, MNRAS, 439, 264
Governato, F., Weisz, D., Pontzen, A., et al. 2015, MNRAS, 448, 792
Graham, P. W., Irastorza, I. G., Lamoreaux, S. K., Lindner, A., & van Bibber, K. A. 2015, ARNPS, 65, 485
Grazian, A., Fontana, A., Santini, P., et al. 2015, A&A, 575, A96
Gruppioni, C., Calura, F., Pozzi, F., et al. 2015, MNRAS, 451, 3419
Guo, Q., White, S., Boylan-Kolchin, M., et al. 2011, MNRAS, 413, 101
Guo, Q., White, S., Li, C., & Boylan-Kolchin, M. 2010, MNRAS, 404, 1111
Heikinheimo, M., Tenkanen, T., & Tuominen, K. 2017, PhRvD, 96, 023001
Henriques, B. M. B., White, S. D. M., Thomas, P. A., et al. 2015, MNRAS, 451, 2663
Herpich, J., Stinson, G. S., Macciò, A. V., et al. 2014, MNRAS, 437, 293
Hirschmann, M., Naab, T., Davé, R., et al. 2013, MNRAS, 436, 2929
Hirschmann, M., Somerville, R. S., Naab, T., & Burkert, A. 2012, MNRAS, 426, 237
Horiuchi, S., Humphrey, P. J., Oñorbe, J., et al. 2014, PhRvD, 89, 025017
Hou, J., Frenk, C. S., Lacey, C. G., & Bose, S. 2016, MNRAS, 463, 1224
Iakubovskyi, D. A. 2016, AASP, 6, 13
Ivezic, Z., Connolly, A. J., & Juric, M. 2016, in IAU Symp. 325, Astroinformatics, ed. M. Brescia et al. (Cambridge: Cambridge Univ. Press), 93

Kang, X., Macció, A. V., & Dutton, A. A. 2013, ApJ, 767, 22
Katz, H., Lelli, F., McGaugh, S. S., et al. 2017, MNRAS, 466, 1648
Kawamata, R., Ishigaki, M., Shimasaku, K., et al. 2017, arXiv:1710.07301
Kennedy, R., Frenk, C., Cole, S., & Benson, A. 2014, MNRAS, 442, 2487
Kimm, T., Somerville, R. S., Yi, S. K., et al. 2009, MNRAS, 394, 1131
Klypin, A. A., Kravtsov, A. V., Valenzuela, O., & Prada, F. 1999, ApJ, 522, 82
König, J., Merle, A., & Totzauer, M. 2016, JCAP, 11, 038
Lacey, C., & Cole, S. 1993, MNRAS, 262, 627
Laporte, N., Streblyanska, A., Kim, S., et al. 2015, A&A, 575, A92
Larson, R. B. 1974, MNRAS, 169, 229
Li, C., & White, S. D. M. 2009, MNRAS, 398, 2177
Livermore, R. C., Finkelstein, S. L., & Lotz, J. M. 2017, ApJ, 835, 113
Lo Faro, B., Monaco, P., Vanzella, E., et al. 2009, MNRAS, 399, 827
Lotz, J. M., Koekemoer, A., Coe, D., et al. 2017, ApJ, 837, 97
Lovell, M. R., Bose, S., Boyarsky, A., et al. 2016, MNRAS, 461, 60
Lovell, M. R., Bose, S., Boyarsky, A., et al. 2017a, MNRAS, 468, 4285
Lovell, M. R., Eke, V., Frenk, C. S., et al. 2012, MNRAS, 420, 2318
Lovell, M. R., Gonzalez-Perez, V., Bose, S., et al. 2017b, MNRAS, 468, 2836
Macció, A. V., Dutton, A. A., & van den Bosch, F. C. 2008, MNRAS, 391, 1940
Macció, A. V., Udrescu, S. M., Dutton, A. A., et al. 2016, MNRAS, 463, L69
Madau, P., & Dickinson, M. 2014, ARA&A, 52, 415
Maio, U., & Viel, M. 2015, MNRAS, 446, 2760
Malyshev, D., Neronov, A., & Eckert, D. 2014, PhRvD, 90, 103506
Marsh, D. J. E. 2016, PhR, 643, 1
Mateo, M. L. 1998, ARA&A, 36, 435
McConnachie, A. W. 2012, AJ, 144, 4
McGee, S. L., Balogh, M. L., Wilman, D. J., et al. 2011, MNRAS, 413, 996
Menci, N., Cavaliere, A., Fontana, A., et al. 2003, ApJL, 587, L63
Menci, N., Fiore, F., & Lamastra, A. 2012, MNRAS, 421, 2384
Menci, N., Fiore, F., & Lamastra, A. 2013, ApJ, 766, 110
Menci, N., Fiore, F., Puccetti, S., & Cavaliere, A. 2008, ApJ, 686, 219
Menci, N., Fontana, A., Giallongo, E., & Salimbeni, S. 2005, ApJ, 632, 49
Menci, N., Gatti, M., Fiore, F., & Lamastra, A. 2014, A&A, 569, 37
Menci, N., Grazian, A., Castellano, M., & Sanchez, N. G. 2016, ApJL, 825, L1
Menci, N., Merle, A., Totzauer, M., et al. 2017, ApJ, 836, 61
Merle, A. 2013, IJMPD, 22, 1330020
Merle, A., & Totzauer, M. 2015, JCAP, 1506, 011
Mo, H. J., Mao, S., & White, S. D. M. 1998, MNRAS, 295, 319
Moore, B., Quinn, T., Governato, F., Stadel, J., & Lake, G. 1999, MNRAS, 310, 1147
Moster, B. P., Somerville, R. S., Maulbetsch, C., et al. 2010, ApJ, 710, 903
Munshi, F., Brooks, A. M., Applebaum, E., et al. 2017, arXiv:1705.06286
Navarro, J. F., Frenk, C. S., & White, S. D. M. 1997, ApJ, 490, 493
Neronov, A., Malyshev, D., & Eckert, D. 2016, arXiv:1607.07328
Nickerson, S., Stinson, G., Couchman, H. M. P., Bailin, J., & Wadsley, J. 2011, MNRAS, 415, 257
Nierenberg, A. M., Treu, T., Menci, N., Lu, Y., & Wang, W. 2013, ApJ, 772, 146
Okamoto, T., Gao, L., & Theuns, T. 2008, MNRAS, 390, 920
Pace, A. B. 2016, arXiv:16050.5326
Papastergis, E., Giovanelli, R., Haynes, M. P., & Shankar, F. 2015, A&A, 574, A113
Papastergis, E., & Shankar, F. 2016, A&A, 591, 58

Parsa, S., Dunlop, J. S., McLure, R. J., & Mortlock, A. 2016, MNRAS, 456, 3194
Peebles, P. J. E. 1993, Principles of Physical Cosmology (Princeton, NJ: Princeton Univ. Press)
Peng, Y., Lilly, S. J., Renzini, A., & Carollo, M. 2012, ApJ, 757, 4
Pierce, C. M., Lotz, J. M., Salim, S., et al. 2010, MNRAS, 408, 139
Polisensky, E., & Ricotti, M. 2011, PhRvD, 83, 043506
Read, J. I., Iorio, G., Agertz, O., & Fraternali, F. 2017, MNRAS, 467, 2019
Ruchayskiy, O., Boyarsky, A., Iakubovskyi, D., et al. 2016, MNRAS, 460, 1390
Sacchi, E., Annibali, F., Cignoni, M., et al. 2016, ApJ, 830, 3
Santini, P., Fontana, A., Grazian, A., et al. 2012, A&A, 538, A33
Santini, P., Maiolino, R., Magnelli, B., et al. 2014, A&A, 526, 30
Sawala, T., Frenk, C. S., Fattahi, A., et al. 2016, MNRAS, 457, 1931
Schneider, A. 2015, MNRAS, 451, 3117
Schneider, A., Smith, R. E., Macció, A. V., & Moore, B. 2012, MNRAS, 424, 684
Schneider, A., Smith, R. E., & Reed, D. 2013, MNRAS, 433, 1573
Schneider, A., Trujillo-Gomez, S., Papastergis, E., Reed, D. S., & Lake, G. 2017a, MNRAS, 470, 1452
Schneider, A., Trujillo-Gomez, S., Papastergis, E., Reed, D. S., & Lake, G. 2017, MNRASb, 470, 1542
Schultz, C., Onorbe, J., Abazajian, K. N., & Bullock, J. S. 2014, MNRAS, 442, 1597
Shen, S., Madau, P., Conroy, C., Governato, F., & Mayer, L. 2014, ApJ, 792, 99
Shi, X. D., & Fuller, G. M. 1999, PhRvL, 82, 2832
Skillman, E. D., & Bender, R. 1995, RMxAC, 3, 25
Somerville, R. S., & Dave', R. 2015, ARA&A, 53, 51
Somerville, R. S., Primack, J. R., & Faber, S. M. 2001, MNRAS, 320, 504
Springel, V., Wang, J., Vogelsberger, M., et al. 2008, MNRAS, 391, 1685
Steffen, F. D. 2006, JCAP, 9, 1
Tomczak, A. R., Quadri, R. F., Tran, K. H., et al. 2014, ApJ, 783, 85
Trujillo-Gomez, S., Schneider, A., Papastergis, E., Reed, D. S., & Lake, G. 2016, arXiv:1610.09335
Urban, O., Werner, N., Allen, S. W., et al. 2015, MNRAS, 451, 244
Venumadhav, T., Cyr-Racine, F.-Y., Abazajian, K. N., & Hirata, C. M. 2016, PhRvD, 94, 043515
Viel, M., Becker, G. D., Bolton, J. S., & Haehnelt, M. G. 2013, PhRvD, 88, 043502
Viel, M., Lesgourgues, J., Haehnelt, M. G., Matarrese, S., & Riotto, A. 2006, PhRvL, 97, 071301
Vincenzo, F., Matteucci, F., de Boer, T. J. L., Cignoni, M., & Tosi, M. 2016, MNRAS, 460, 2238
Wang, L., Gonzalez-Perez, V., Xie, L., et al. 2017, MNRAS, 468, 4579
Wang, W., Jiaxin, A., Cooper, A. P., et al. 2015, MNRAS, 453, 377
Weinmann, S. M., Pasquali, A., Oppenheimer, B. D., et al. 2012, MNRAS, 426, 2797
Wetzel, A. R., Tinker, J. L., & Conroy, C. 2012, MNRAS, 424, 232
Wetzel, A. R., Tinker, J. L., Conroy, C., & van den Bosch, F. C. 2013, MNRAS, 432, 336 (W13)
Wheeler, C., Oñorbe, J., Bullock, J. S., et al. 2015, MNRAS, 453, 1305
Yang, X., Mo, H. J., van den Bosch, F. C., et al. 2007, ApJ, 671, 153
Yang, X., Mo, H. J., van den Bosch, F. C., & Jing, Y. P. 2005, MNRAS, 356, 1293
Zavala, J., Jing, Y. P., Faltenbacher, A., et al. 2009, ApJ, 700, 1779